Chem Catalysis

CellPress

Article

Controlled proton accessibility through carboxylic-based organic ligands for highly efficient and selective ammonia electrosynthesis

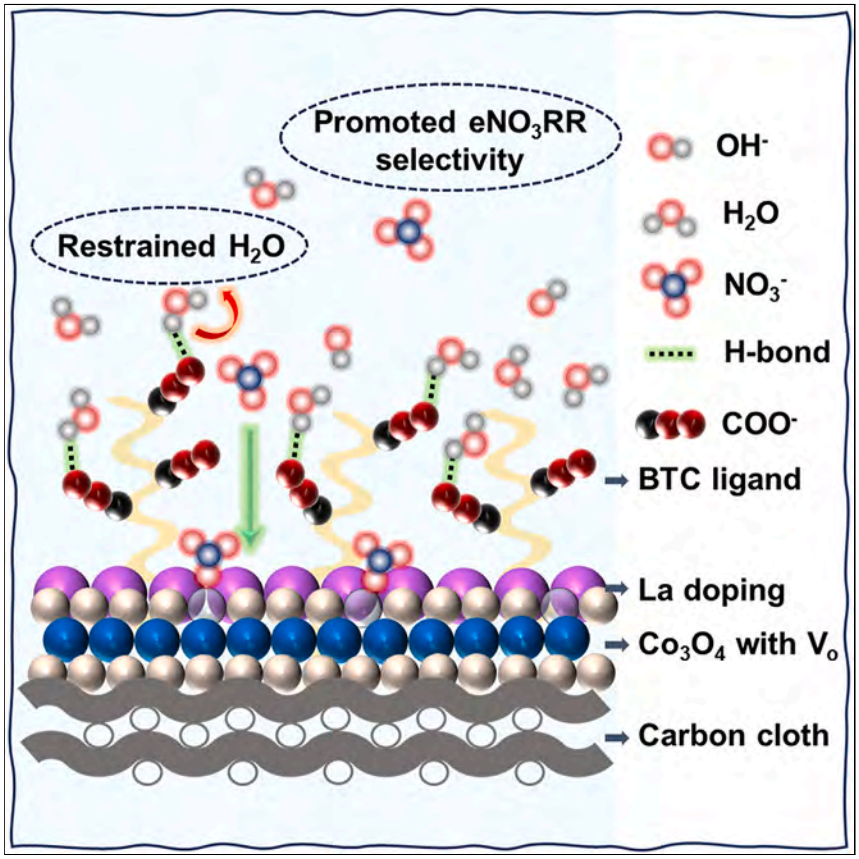

A remarkable electrocatalyst comprising Co_3O_4 nanoparticles modified with doped La atoms and carboxylic-based organic ligands designed to regulate proton accessibility and suppress competing hydrogen evolution reaction in electrochemical nitrate reduction (eNO_3RR).

Dong Chen, Shaoce Zhang, Di Yin, ..., Takeshi Yanagida, Chunyi Zhi, Johnny C. Ho

yip.sen.po.472@m.kyushu-u.ac.jp (S.Y.)
johnnyho@cityu.edu.hk (J.C.H.)

Highlights

Carboxylic-based organic ligands-functionalized electrocatalyst

Lanthanum doping introduces active sites with strong affinity for nitrate ions

Carboxylic-based groups form hydrogen bonds with free water

Controlling proton accessibility suppresses competing hydrogen generation

Chen et al., Chem Catalysis 4, 101024
July 18, 2024
https://doi.org/10.1016/j.checat.2024.101024

Chem Catalysis

CellPress

Article

Controlled proton accessibility through carboxylic-based organic ligands for highly efficient and selective ammonia electrosynthesis

Dong Chen,[1] Shaoce Zhang,[1] Di Yin,[1] Quan Quan,[1] Yuxuan Zhang,[1] Weijun Wang,[1] You Meng,[1,2] Xueda Liu,[5] SenPo Yip,[3,*] Takeshi Yanagida,[3,4] Chunyi Zhi,[1] and Johnny C. Ho[1,2,3,6,*]

SUMMARY

Competing hydrogen evolution reaction (HER) and sluggish multi-electron/proton-involved steps are the major obstacles to improving the efficiency and selectivity of electrochemical nitrate reduction to ammonia (eNO_3RR). Herein, we modified Co_3O_4 nanoparticles with doped rare-earth La atoms and carboxylic (COO^-)-based organic ligands. The COO^- groups efficiently reduce the water activity around the active sites by forming hydrogen bonds, thus controlling proton accessibility and regulating the adsorption selectivity between nitrate ions and protons. Simultaneously, introducing oxygen vacancies through La doping establishes active sites with a strong affinity for nitrate ions and an electron-rich local environment conducive to eNO_3RR. The electrocatalyst exhibits superior activity and selectivity with an ammonia Faradaic efficiency of up to 99.41% and a yield rate of 5.62 mg h^{-1} mg_{cat}^{-1} at −0.3 V vs. reversible hydrogen electrode (RHE). Notably, the catalyst maintains over 90% Faradaic efficiency for NH_3 production across a broad potential range of 400 mV, surpassing most recently reported eNO_3RR electrocatalysts.

INTRODUCTION

Ammonia (NH_3) is paramount as a widely produced chemical, playing a vital role as building blocks across diverse products, including fertilizers, textiles, and pharmaceuticals.[1] The most typical method for industrialized NH_3 production relies on the Haber-Bosch process, which demands the fusion of nitrogen (N_2) and hydrogen (H_2) under formidable conditions of high pressure (200–350 atm) and temperature (400°C–600°C), and large amounts of carbon dioxide (CO_2) are inevitably generated.[2,3] Due to the burgeoning environmental concerns, extensive research is being performed to explore alternative green routes for NH_3 production, such as electrochemical reduction from N_2 or nitrate (NO_3^-).[4,5] However, the low NH_3 production rate of electrochemical N_2 reduction accentuates the interest in NO_3^- reduction.[6,7] Meanwhile, NO_3^- usually exists in industrial and agricultural wastewater, leading to environmental and health issues.[8,9] The incomplete conversion of NO_3^- into nitrites (NO_2^-) also brings health concerns, while the reduction into N_2 is energy intensive (about 11.7–12.5 kWh kg N^{-1}),[10] so electrochemical nitrate reduction reaction to NH_3 (eNO_3RR) become a significant scientific research hotspot. The eNO_3RR meets the requirements for removing nitrate ions from wastewater and efficiently produces high-value-added NH_3.[11] Nevertheless, the rational design of electrocatalysts for eNO_3RR with both high selectivity and activity is still lacking, especially since there is a competing hydrogen evolution reaction (HER) that is only a two-electron transfer process.[12]

THE BIGGER PICTURE

Ammonia, the second most popular commercialized synthetic chemical in the world, is widely used for fertilizer and production of all nitrogen-atom-containing chemicals. Electrochemical nitrate reduction reaction (eNO_3RR) offers a green and appealing approach to sustainable ammonia synthesis. However, it is hindered by the multi-proton-coupled electron transfer steps and competitive hydrogen evolution reaction (HER). To this end, keeping an appropriate equilibrium of electron and proton accessibility kinetics around the active sites of catalysts emerges as a crucial principle to enhance the activity and selectivity of eNO_3RR. In this work, we demonstrate that the carboxylic-based organic ligands on metal oxides could form hydrogen bonds with water, effectively diminish water activity, and control the proton accessibility, thus achieving a highly efficient and selective ammonia electrosynthesis.

In general, the eNO_3RR process involves three stages: (1) the adsorption of NO_3^- on the active sites, (2) the continuous proton-coupled electron transfer (PCET) steps including nine protons and eight electrons ($NO_3^- + 9H^+ + 8e^- \rightarrow NH_3 + 3H_2O$ in acidic and neutral electrolytes or $NO_3^- + 6H_2O + 8e^- \rightarrow NH_3 + 9OH^-$ in alkaline electrolytes), followed by (3) the formation and desorption of NH_3 molecules.[13–15] Basically, the adsorption and desorption rely on the intrinsic activity of the active sites, while PCET steps mainly depend on the electron and proton accessibilities.[16,17] Besides, the competing HER that lies on the adsorption priority of NO_3^+ and H^+ on active sites also significantly influences the eNO_3RR rate. Therefore, it follows that the electron and proton accessibility-kinetic profoundly governs the pace of the PCET step and remains pivotal in curtailing the generation of undesirable by-products, such as H_2. For example, semimetals such as Sn and Bi have recently been introduced as sub/monolayer second metals on the electrodes to suppress HER and promote nitrate adsorption due to the reported limited electron transfer and weakened hydrogen binding on the surface.[18–20] Nonetheless, an excessive hindrance of electron or proton supply unavoidably results in a shortage of essential resources for the eNO_3RR process. In this regard, keeping an appropriate equilibrium of electron and proton accessibility kinetics at the surface of catalysts emerges as a crucial principle. This principle offers valuable direction for current research and development efforts on the optimal design of eNO_3RR electrocatalysts with high activity and selectivity.

With regard to the competing HER, although nitrate reduction can happen at an overpotential lower than HER, the reaction would then occur under a small current density, and the NH_3 synthesis remains considerably distant from achieving an industrial scale.[21,22] This discrepancy underscores a crucial challenge: effectively curb hydrogen generation while achieving increased NH_3 production under high overpotentials. Recent strides in research have entailed the introduction of additives, such as dimethyl sulfoxide (DMSO), hydrophilic polyethylene glycol (PEG), and glucose, into the aqueous electrolyte.[23–25] This strategic modification diminishes water activity by forming hydrogen bonds (H-bonds) between the additives and the free water molecules. However, the eNO_3RR process still depends on water splitting in aqueous media as a proton donor to supply continual generation of active adsorbed hydrogen (*H [the asterisk represents the active sites]), which needs to be regulated to a balanced level. Electrolyte additives, especially in high concentrations, can easily go beyond the limit and thus retard the water splitting. Consequently, rational strategies must be developed to control HER rate but not affect proton supply. Inspired by the function of organic electrolyte additives, organic molecule ligands or even organic molecules have attracted intensive interest in electrocatalysis. This paradigm shift toward organic molecules underlines their promise in addressing the intricate balance between HER control and maintaining an adequate proton reservoir. For instance, Chen et al. reported an excellent performance of a single ethylenediaminetetraacetic acid (EDTA) molecular catalyst for reducing CO_2 to CH_4.[26] They found that the Lewis basic carboxylic (COO^-) groups act as the active sites for CO_2 reduction and have favorable energy for the hydrogenation of *CO to the reduced product of CH_4. Despite density functional theory (DFT) calculations proving the excellent electrocatalysis performance of organic molecules in these works, there are few reports on the application of eNO_3RR. Furthermore, challenges remain in terms of how the organic functional groups affect the electronic structure of active sites and the transfer of protons, and the relationship between the selectivity of eNO_3RR and suppressed HER is still ambiguous.

In this work, we take the electron-rich carboxylate functional group as an example and elucidate the significant effect of carboxylate groups on confining the water

[1]Department of Materials Science and Engineering, City University of Hong Kong, Hong Kong, Hong Kong SAR 999077, China

[2]State Key Laboratory of Terahertz and Millimeter Waves, City University of Hong Kong, Hong Kong, Hong Kong SAR 999077, China

[3]Institute for Materials Chemistry and Engineering, Kyushu University, Fukuoka 816–8580, Fukuoka, Japan

[4]Department of Applied Chemistry, Graduate School of Engineering, The University of Tokyo, Tokyo 113-8656, Bunkyo, Japan

[5]Interdisciplinary Graduate School of Engineering Sciences, Kyushu University, Fukuoka 816-8580, Japan

[6]Lead contact

*Correspondence: yip.sen.po.472@m.kyushu-u.ac.jp (S.Y.), johnnyho@cityu.edu.hk (J.C.H.)

https://doi.org/10.1016/j.checat.2024.101024

activity, facilitating nitrate adsorption, and balancing the PCET steps in eNO_3RR. Lanthanum (La), a rare-earth element, is doped into Co_3O_4 nanoparticles (NPs). Taking advantage of a larger ionic radius than Co, unique Lewis acid characteristics, and high coordination number of La, the La doping leads to the lattice disorder of Co_3O_4 NPs and generates abundant oxygen vacancies (O_v) while serving as a bridge to combine Co_3O_4 with carboxylic-based organic ligands, which function as Lewis bases.[27] Electrochemical *in situ* measurements, including attenuated total reflection surface-enhanced infrared absorption spectroscopy (ATR-SEIRAS) measurement, Raman spectroscopy measurement, and differential electrochemical mass spectrometry (DEMS) test as well as density functional theory (DFT) calculations and molecular dynamics (MD) simulations conducted to demonstrate the reduced water activity and clarify the PCET mechanisms and pathways during eNO_3RR. The resulting carboxylate-functionalized La-doped Co_3O_4 catalysts exhibit superior catalytic performances, (1) exhibiting a Faradaic efficiency (FE) as high as 99.41% with an NH_3 yield rate of 5.62 mg h^{-1} mg_{cat}^{-1} at −0.3 V vs. reversible hydrogen electrode (RHE), (2) achieving the NH_3 yield rate of 31.24 mg h^{-1} mg_{cat}^{-1} at −0.7 V vs. RHE, and (3) possessing a wide potential window (400 mV, from −0.3 to −0.7 V) for NH_3 production with >90% FE, which is top-ranked among the electrocatalysts for eNO_3RR so far. This work provides a rational strategy based on organic carboxylic ligands for the high NH_3 production rate. More importantly, the findings can contribute to subsequent catalyst optimization and scaling up in other electrochemical techniques with HER as a competition reaction, such as CO_2 reduction.

RESULTS AND DISCUSSION

Synthesis and structural characterizations

Co_3O_4 NPs were synthesized by a simple coprecipitation method, employing cobalt nitrate hexahydrate ($Co(NO_3)_2 \cdot 6H_2O$) and sodium hydroxide (NaOH) as reactants. The La-doped Co_3O_4 catalysts with rich oxygen vacancies (La-Co_3O_{4-x}) were fabricated using an identical procedure, with the exception that lanthanum nitrate hexahydrate ($La(NO_3)_3 \cdot 6H_2O$) was included in the precursor. The abbreviation La_y-Co_3O_{4-x} (where y = 3, 6, and 9) represents Co_3O_{4-x} with different La doping concentrations of 3.02, 6.29, and 9.11 atom % (La-Co_3O_{4-x} represents La_9-Co_3O_{4-x} in the following). Figure 1A depicts the schematic illustration of the crystal structure evolution of Co_3O_4 studied here. The spinel Co_3O_4 adopts the standard spinel structure with Co^{2+} ions in the tetrahedral coordination centers (A_{td}, yellow block) and Co^{3+} ions in the octahedral interstices (B_{oh}, violet block), thus allowing the Co_3O_4 crystal with internal corner-sharing A_{td}−O−B_{oh} and edge-sharing B_{oh}−O−B_{oh} configurations.[28,29] As reported, the substitution of Co^{3+} by La^{3+} for the occupation of the B_{oh} sites occurs more readily. However, the significant mismatch of the ionic radius between La^{3+} and Co^{3+} may result in strong lattice strain, thereby leading to the rearrangement of A_{td} and B_{oh} sites and the formation of oxygen vacancies (O_v).[30] DFT calculations have been utilized to determine the formation energy in both substitution situations (Figure S1). The outcomes coincide with previously reported findings, affirming that the replacement of B_{oh} by La yields lower formation energy than the A_{td} substitution. After that, we choose benzenetricarboxylic acid (H_3BTC) with three carboxylates as carboxylic organic ligands. Leveraging the unique Lewis acid attributes and high coordination number of the rare-earth element La,[31] its incorporation serves as a bridging mechanism connecting the carboxylate functional ligand with Co_3O_4 (abbreviated as BTC/La-Co_3O_{4-x}, in which La-Co_3O_{4-x} represents La_9-Co_3O_{4-x}). The as-prepared BTC/La-Co_3O_{4-x} NPs show an average size of 14.37 ± 5.28 nm, which is a little smaller than that of Co_3O_4 NPs (19.97 ± 7.10 nm), resulting from the larger ionic radius of dopant atoms than host atoms (Figures 1B, 1C,

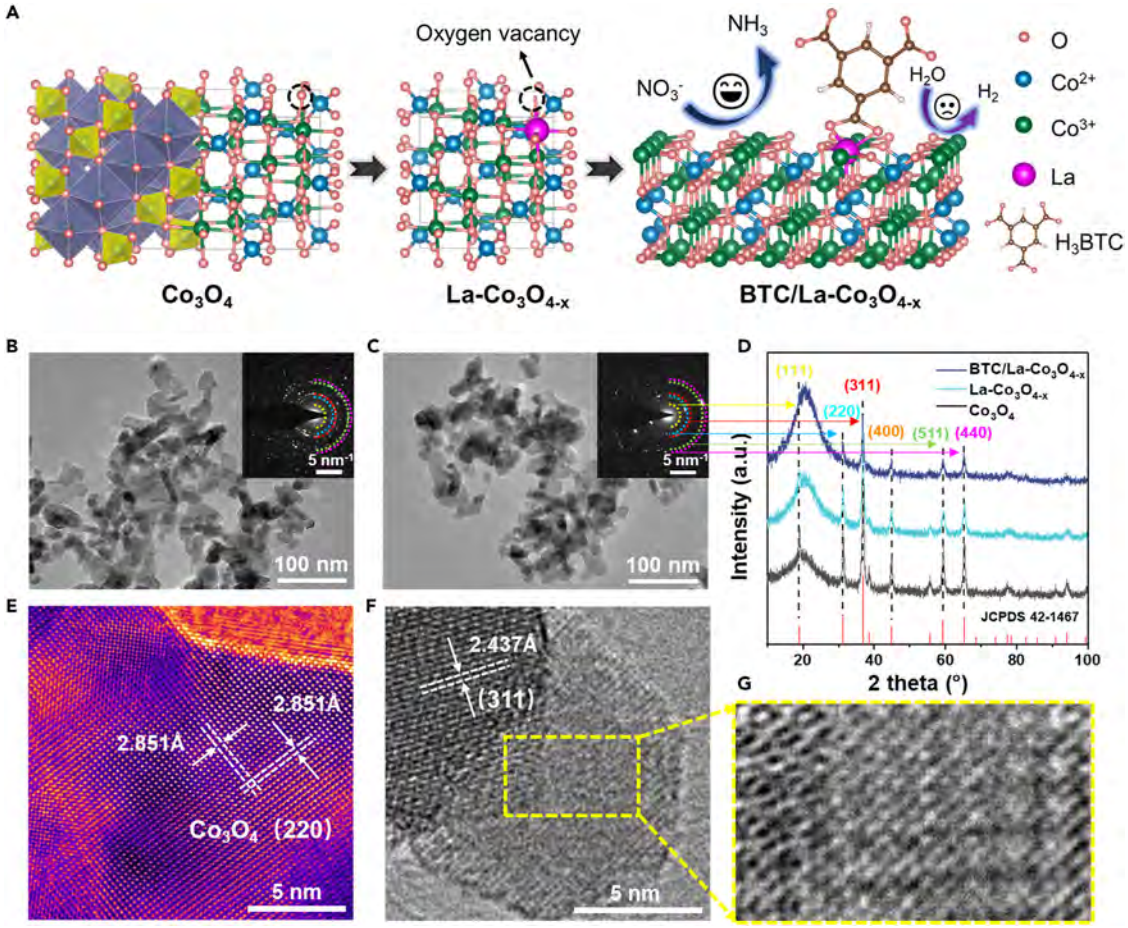

Figure 1. Schematic illustration and structural characterization for the preparation of BTC/La-Co_3O_{4-x} and reference materials

(A) Schematic illustration of the crystal structures of Co_3O_4, La-Co_3O_{4-x}, and BTC/La-Co_3O_{4-x}.

(B) TEM image of Co_3O_4, and the inset shows the corresponding SAED pattern.

(C) TEM image of BTC/La-Co_3O_{4-x}, and the inset shows the corresponding SAED pattern.

(D) XRD patterns of Co_3O_4, La-Co_3O_{4-x}, and BTC/La-Co_3O_{4-x}.

(E) HRTEM image of Co_3O_4.

(F) HRTEM image of BTC/La-Co_3O_{4-x}.

(G) Inverse FFT image from the region circled by the yellow dashed box in (F).

and S2).[32] The insets in Figures 1B and 1C are the corresponding selected area electron diffraction (SAED) patterns, revealing that the lattice spacings of both the samples are well consistent with the cubic phase of Co_3O_4 (JCPDS 42–1467) in the X-ray diffraction (XRD) patterns and no other La-based compounds are formed (Figure 1D). Based on Figure S3A, it is important to highlight that the peak intensities significantly decrease as the La doping content increases, along with the introduction of BTC ligands. This phenomenon arises due to the differing electron densities between the introduced atoms (La atoms) and their surrounding counterparts, reducing crystallinity and increasing defect occurrence.[32] Additionally, the amplified area from Figure S3A shows a slight peak shift to a lower angle with the increased La doping because the lattice expansion resulted from the replacement of Co^{3+} by La^{3+} with a bigger ionic radius.[33] The g-value signals at 2.002 of electron paramagnetic resonance (EPR) related to oxygen vacancies are detected for La_y-Co_3O_{4-x}, verifying the formation of O_v due to the La doping (Figure S3B).[34] Additionally, this augmented O_v content is also shown by the reduced Raman peak intensity and broader peak

width in Figure S4.[35] Figures 1E and S5 display the high-resolution transmission electron microscopy (HRTEM) image of pure Co_3O_4 NPs, which indicates good crystallinity with typical (220) facets in the cubic phase. Upon modification with La atoms and BTC ligands, although the lattice spacings of the Co_3O_4 (311) plane of 2.437 Å are discernible, a majority of the lattice fringes become less distinctive (Figures 1F and S6). These dislocations and distortions are even more apparent following the application of an inverse fast Fourier transform (FFT) mask to the selected region, further demonstrating the incorporation of numerous O_v defects within the lattice (Figure 1G). These O_v defects equalize electron distribution, compensating for the uneven electron density resulting from La doping and leading to unsaturated coordination at both La and Co sites. This distribution ensures the requisite coordination environment for BTC ligands, culminating in a substantial augmentation of active sites,[36] which will be substantiated by subsequent experimental investigations.

The zeta (ζ) potential represents the charge that develops at the boundary between an NP surface and the surrounding liquid medium. It stands as an important technique for comprehending the state of the NP surface.[37,38] As shown in Figure 2A, both pure Co_3O_4 and H_3BTC show a negative charged surface in aqueous solution (pH = 7). Under La doping, the ζ potential of Co_3O_4 NPs transforms from −3.85 to 1.47 mV, manifesting the emergence of the positively charged surface due to the generated surface O_v, which is also beneficial for the combination of electron-rich BTC ligands owing to electrostatic attraction force.[39] As for BTC/La-Co_3O_{4-x}, the ζ potential of 1.07 mV is smaller than that of La-Co_3O_{4-x} because of the addition of negative electrons from the COO^- of BTC ligands. Despite this, the ζ potential remains predominantly positive on the surface of BTC/La-Co_3O_{4-x}, ensuring favorable electrostatic adsorption toward NO_3^- during eNO_3RR. Furthermore, Fourier transform infrared (FTIR) and Raman spectra were conducted to validate the presence of BTC ligands (Figures 2B and 2C). In addition to the two absorption FTIR peaks at 549 and 658 cm^{-1}, which correspond to the Co–O bond in the spinel lattice, representing Co^{3+} in an octahedral hole, and the O–Co–O bond of Co^{2+} in a tetrahedral site, respectively, two distinct peaks at 1,366 and 1,557 cm^{-1} are observable, which are from symmetric and asymmetric vibrations of $–COO^-$ (Figure 2B).[40,41] Additionally, two relatively subtle peaks located at 1,436 and 1,669 cm^{-1}, signifying the vibrations of –COOH, are observed.[42] These observations align with the characteristic peaks of H_3BTC. In the meantime, the obvious doublet Raman bands around 1,446 and 1,634 cm^{-1} are shown in BTC/La-Co_3O_{4-x} (Figure 2C), belonging to the stretching modes of uncoordinated carboxylate groups. It is noteworthy that these two peaks of stretching modes are broad, which cover the moiety of $–COO^-$ groups located at 1,610 and 1,424 cm^{-1}.[43] Furthermore, the high-angle annular dark-field (HAADF) image and energy dispersive spectrometry (EDS) elemental mapping (Figure 2D), scanning electron microscope (SEM)-energy dispersive X-ray (EDX) spectra, and EDS elemental mapping (Figures S7, S8, S9, and S10) demonstrate a uniform distribution of La and C elements throughout the samples after La doping and H_3BTC combination. The above results, taken together, confirm the successful synthesis of La_y-Co_3O_{4-x} and BTC/La-Co_3O_{4-x} NPs.

More importantly, the electronic structures and local environment are explored by the charge density differences, Bader charge, X-ray photoelectron spectroscopy (XPS), and X-ray absorption spectroscopy for the catalysts. As depicted in Figures 2E and S11, La-Co_3O_{4-x} exhibits robust electronic interactions around the La atom, donating 0.16e to neighboring O atoms. Furthermore, a conspicuous charge depletion is observable in the O_v region, while the electrons accumulate at

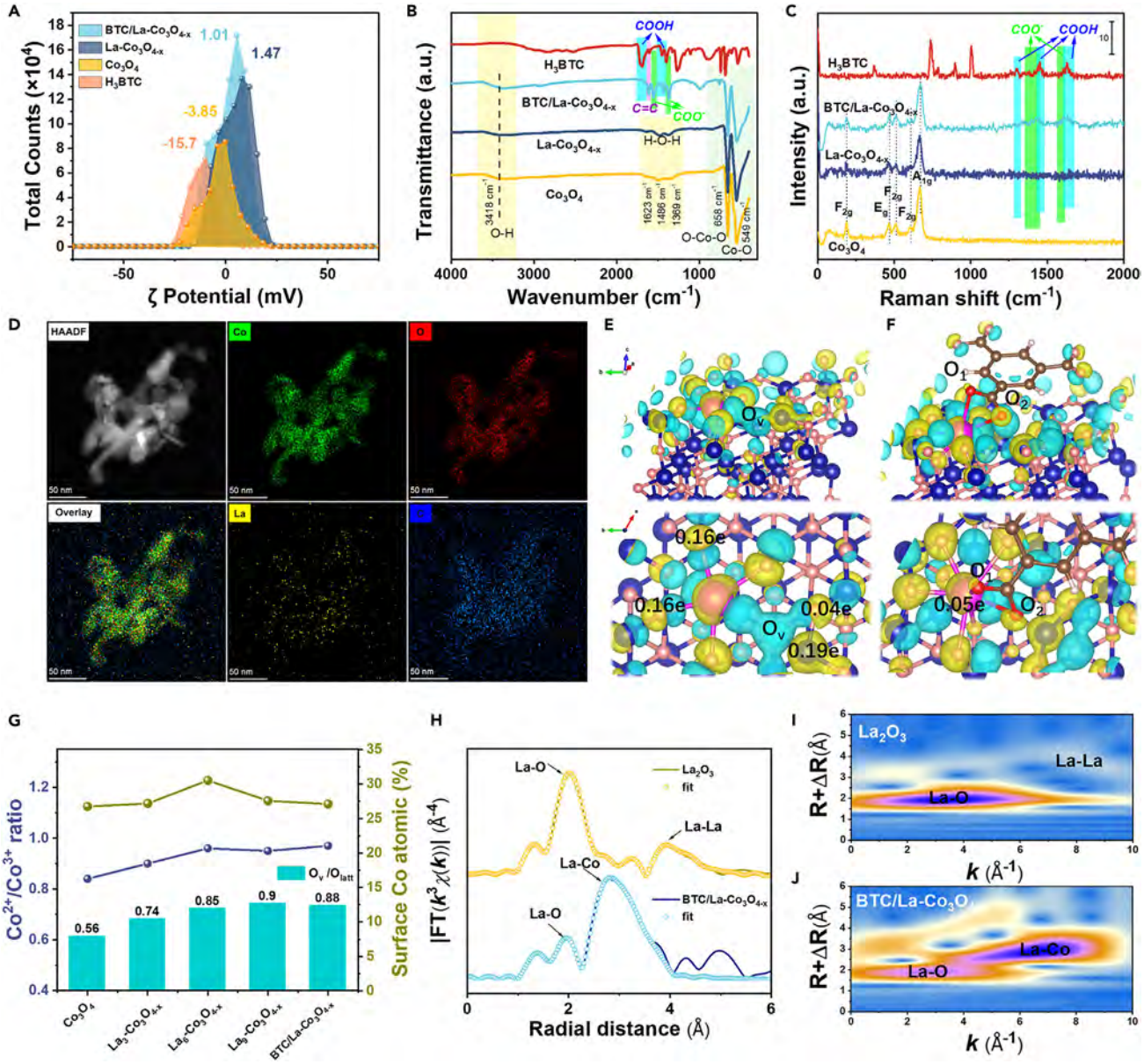

Figure 2. Characterization of the BTC ligand and electronic microenvironment of BTC/La-Co_3O_{4-x} and reference materials

(A) Zeta (ζ) potential in aqueous solution (pH = 7).

(B) FTIR spectra.

(C) Raman spectra.

(D) HAADF image and EDS elemental mapping of BTC/La-Co_3O_{4-x}.

(E) Charge density differences and charge transfer of La-Co_3O_{4-x} with the cyan and yellow colors designating the depletion and accumulation of charge density.

(F) Charge density differences and charge transfer of BTC/La-Co_3O_{4-x} with the cyan and yellow colors designating the depletion and accumulation of charge density.

(G) The Co^{2+}/Co^{3+} atomic ratio, surface Co atomic ratio, and O_v/O_{latt} ratio on the surface of the samples.

(H) The k^3-weighted Fourier transform spectra from La L3 edge EXAFS in R space.

(I) Wavelet-transformed k^3-weighted EXAFS spectra of La_2O_3.

(J) Wavelet-transformed k^3-weighted EXAFS spectra of BTC/La-Co_3O_{4-x}.

the adjacent Co and neighboring O atoms in the visual area, of which electron transfer is calculated to be 0.19e and 0.04e. Combined with the BTC ligands, the La atoms serve as a bridge to connect the two O atoms (O_1 and O_2 in Figure 2F) in BTC with the

O atoms in the Co_3O_4 lattice (Figures 2F and S11). The quantitative amount of electron transfers from BTC to Co_3O_4 is confirmed to be 0.05e. The abundant electrons around the La−O_v−Co sites make it more available to adsorb NO_3^- due to the sufficient electron supply for back-donating to the antibonding of NO_3^- orbitals.[35,44] These results verify that introducing La atoms and BTC ligands can modulate the catalysts' electronic structure and charge redistribution, thus, in turn, orchestrating a regulation of the local environment conducive to facilitating efficient nitrate reduction activity. Moreover, the high-resolution Co 2p XPS spectra could be deconvoluted into Co $2p_{3/2}$ and Co $2p_{1/2}$ (779.5 and 794.6 eV for Co^{3+}, 780.8 and 795.9 eV for Co^{2+}) associated with their satellite peaks (Figure S12A).[45] With the increased doping content of La, the samples exhibit pronounced La $3d_{5/2}$ and $3d_{3/2}$ core peaks attributed to the La^{3+} species (Figure S13).[46] Besides, the O 1s XPS spectra could be fitted into three prominent peaks at binding energies of about 529.8, 531.5, and 533.3 eV, assigned to the lattice oxygen (O_{latt}), oxygen atoms next to their vacancies (O_v), and oxygen in the molecular water or hydroxyl species adsorbed on the catalyst surface (O_{ads}), respectively (Figure S12B).[36] Notably, additional peaks at 530.3 and 532.0 eV in BTC/La-Co3O4-x suggest that the oxygen in C=O and C–O bonds to the carboxylic groups in BTC ligands.[47] Remarkably, a reduction in the binding energies is discernible within the Co 2p and O 1s peaks of La_y-Co_3O_{4-x}. This shift indicates the electron transfer from the doped La to the host Co_3O_4 NPs, which is in agreement with the calculated results of charge density differences.[48] By estimating the XPS data, we construct a correlation of the surface Co atom %, Co^{2+}/Co^{3+}, and O_v/O_{latt} ratios as a function of the La contents and the incorporation of BTC in BTC/La-Co_3O_{4-x} in Figures 2G and S14 and Table S1. Firstly, the surface Co atom % displays a volcano plot, accompanied by an approximate upward trend in both the Co^{2+}/Co^{3+} and O_v/O_{latt} ratios with the increased La doping contents, signifying the substituted Co^{3+} by La^{3+} and the formation of O_v. In particular, La_9-Co_3O_{4-x} has the highest O_v/O_{latt} ratio in comparison with pure Co_3O_4, La_3-Co_3O_{4-x}, and La_6-Co_3O_{4-x}, implying the abundant surface O_v induced by the doped La atoms, creating adequate sites for adsorbing the BTC ligands. Therefore, the following investigations choose La_9-Co_3O_{4-x} as the object. To further confirm the doping of La, X-ray absorption near-edge structure (XANES) and extended X-ray absorption fine structure (EXAFS) spectroscopy are performed in Figures 2H–2J and S15. The close absorption edge energy of normalized XANES spectra for BTC/La-Co_3O_{4-x} and reference La_2O_3 indicates the +3 valence state of La in BTC/La-Co_3O_{4-x}. Furthermore, the k^3-weighted Fourier transform spectra in R space and the wavelet transform simulations in k space both indicate the doping of La, with only La-O and La-Co coordination structure in the coordination shell and no La-La scattering path (about 3.8 Å in La_2O_3) can be identified in BTC/La-Co_3O_{4-x}, which clearly prove that La is atomic distributed into the lattice of Co_3O_4. Meanwhile, the fitting results in Table S2 show that the coordination number for La-O in BTC/La-Co_3O_{4-x} is about 5.4, which is close to but lower than the six coordination in CoO_6 octahedron in Co_3O_4, providing direct evidence for the replaced Co^{3+} and generated oxygen vacancies.[49] Collectively, these findings offer compelling evidence of electron redistribution and the resultant modulation of the local environment ensuing from the incorporation of La and BTC ligands, laying the foundation for the favorable adsorption energy of $*NO_3$ and fast conversion from $*NO_3$ to $*NO_2$.

Electrochemical activity and kinetics of eNO_3RR

We then explore the electrochemical performance of eNO_3RR and evaluate the synergistic effects between La doping and BTC ligands. We detect the potential products using the colorimetric method (Figures S16–S18). Initially, we conduct linear sweep voltammetry (LSV) on all the prepared electrocatalysts in the electrolyte

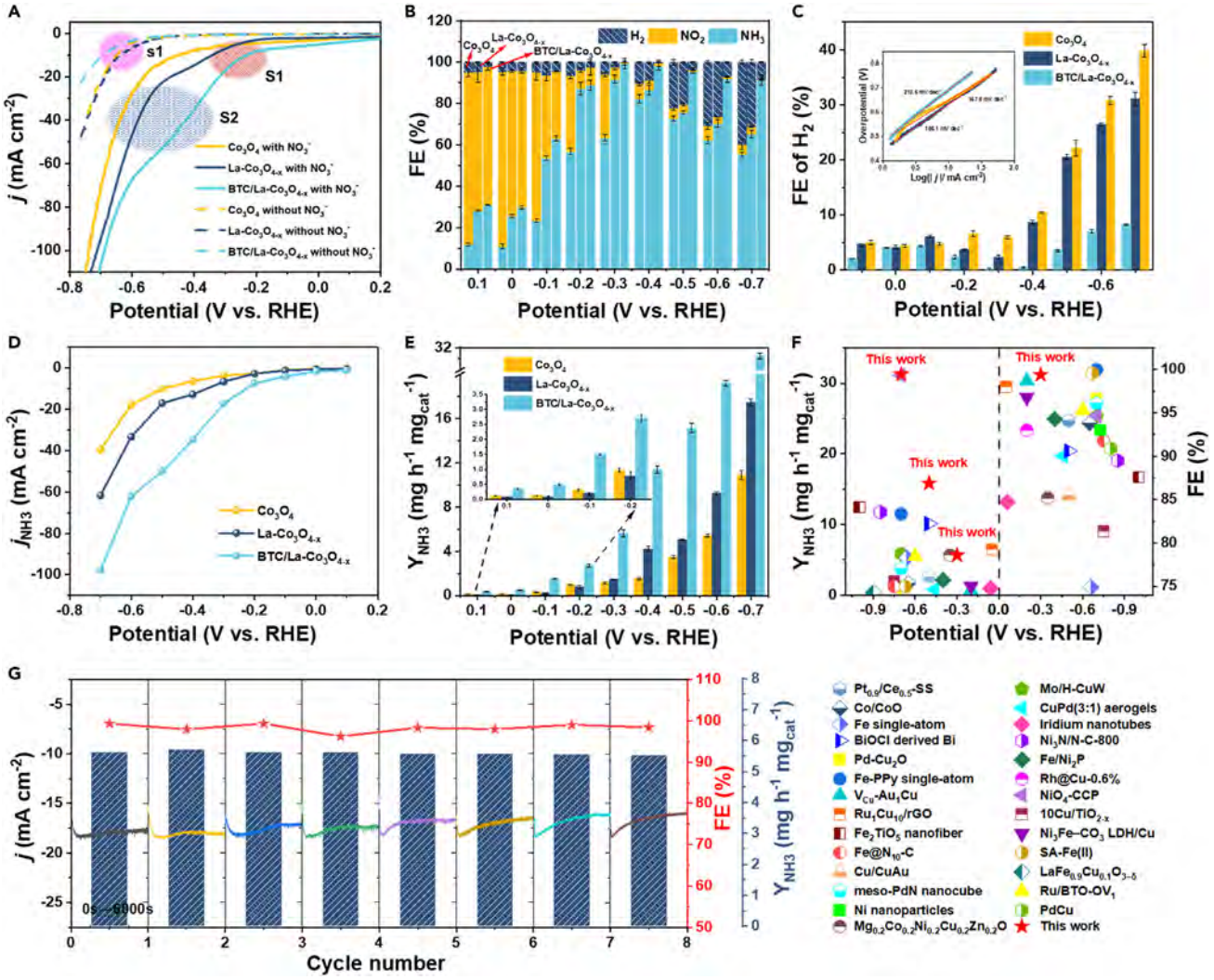

Figure 3. eNO$_3$RR performance of the catalysts

(A) LSV curves.

(B) Faradaic efficiencies (FEs) for NH_3, NO_2, and H_2. Error bars represent the standard deviation from three same samples for testing three times.

(C) FE for H_2; the inset shows the Tafel slopes during HER. Error bars represent the standard deviation from three same samples for testing three times.

(D) Partial current densities of NH_3 (j_{NH3}).

(E) Yield rate for NH_3 (Y_{NH3}). Error bars represent the standard deviation from three same samples for testing three times.

(F) Comparison of Y_{NH3} and FE_{NH3} of BTC/La-Co_3O_{4-x} NPs with the recently reported representatives eNO$_3$RR electrocatalysts at different potentials (see also Table S3).

(G) Time-dependent current density curves and corresponding Y_{NH3} and FE_{NH3} over BTC/La-Co_3O_{4-x} NPs at −0.3 V vs. RHE for eight cycles.

with/without NO_3^- (Figure 3A). Within the current density curves, several spinodal or peaks are observed, indicative of three primary reactions designated as s1, S1, and S2.[50,51]

$$s1 : 2^*H^+ + 2e^- \rightarrow H_2 \quad \text{(Equation 1)}$$

$$S1 : {}^*NO_3^- + H_2O + 2e^- \rightarrow {}^*NO_2^- + 2OH^- \quad \text{(Equation 2)}$$

$$S2 : {}^*NO_2^- + 5H_2O + 6e^- \rightarrow NH_3 + 7OH^- \quad \text{(Equation 3)}$$

Upon the presence of NO_3^-, the current densities drastically increase compared to that in the electrolyte without NO_3^-. Notably, BTC/La-Co_3O_{4-x} and La_y-Co_3O_{4-x} display higher current densities than pure Co_3O_4, suggesting the efficient eNO_3RR activity of the electrocatalysts facilitated by the modification of La doping and BTC ligands (Figure S19). Additionally, all electrocatalysts demonstrate a consistent onset potential at 0.2 V vs. RHE during nitrate reduction. Within the potential range from −0.15 to −0.35 V vs. RHE, the peak labeled as S1 is attributed to the conversion from $*NO_3$ to $*NO_2$ through two PCET steps. Given the negligible contribution of HER within this potential range, the Tafel slopes have been extracted from Figure 3A to elucidate the reaction rate of $*NO_3$-to-$*NO_2$ conversion. As illustrated in Figure S20, the Tafel slopes of Co_3O_4, La-Co_3O_{4-x}, and BTC/La-Co_3O_{4-x} are determined to be 1,027.57, 288.79, and 278.87 mV decade^{-1}, respectively. These findings illustrate the high concentration of O_v displays a higher capability for reducing $*NO_3$ to $*NO_2$, which serve as active sites and provide abundant electrons for reducing nitrate. At the same time, the contribution of BTC ligands in this process is comparatively modest. The electrochemical impedance spectra provide further evidence of fast electron transfer attributed to La doping (Figure S21). As anticipated, the charge transfer resistance is markedly reduced for La-Co_3O_{4-x} (53.68 Ω) and BTC/La-Co_3O_{4-x} (46.42 Ω) in comparison to pristine Co_3O_4 NPs (66.34 Ω). As the potential becomes progressively negative in the LSV curves, the peaks marked as S2 come to the forefront. These peaks correspond to the reduction from $*NO_2^-$ to NH_3, continuing until the onset of HER. As is known, the eNO_3RR involves several by-products, including NO_2^-, NH_3, and hydrazine hydrate (N_2H_4). The results of colorimetry highlight the NH_3 and NO_2^- species as the principal products throughout the eNO_3RR process in this system, while the yield of N_2H_4 is negligible. As depicted in Figure 2B, the La-doped samples significantly enhance the FE of NH_3 (FE_{NH3}) compared to pure Co_3O_4, particularly by diminishing the production of NO_2^-, which is consistent with the LSV results that the La-Co_3O_{4-x} has a fast $*NO_3$-to-$*NO_2$ activity. Subsequent co-modification with BTC ligands further elevates the eNO_3RR performance, demonstrating an outstanding FE_{NH3} of 99.41% at −0.3 V vs. RHE, surpassing that of La-Co_3O_{4-x} (91.77%) and Co_3O_4 (63.44%). More importantly, such high FE_{NH3} (>90%) could maintain at a broad potential range (−0.3 ∼ −0.7 V vs. RHE), whereas the FE_{NH3} for La-Co_3O_{4-x} and Co_3O_4 distinctly declines. At high potentials, it is recognized that the two-electron transfer HER competes with the eight-electron transfer eNO_3RR (s1 region). Consequently, in most electrocatalysts, intensified hydrogen generation emerges as the potential becomes increasingly negative, impeding the eNO_3RR selectivity.[52,53] However, the FE_{H2} for BTC/La-Co_3O_{4-x} NPs is notably suppressed compared to the counterparts, keeping a low value below 10% (Figure 3C). The Tafel slopes of the HER, as seen in the inset, are derived from the s1 region in Figure 3A, of which the much bigger slope of BTC/La-Co_3O_{4-x} (210.5 mV decade^{-1}) means the inherently poor HER activity. This phenomenon is attributed to the constrained activity of free water around the active sites, which comes from establishing H-bonds between the carboxylate groups in BTC ligands and free water molecules. This bonding arrangement subsequently regulates the accessibility and kinetics of protons for the PCET steps and thus affects the selectivity of eNO_3RR. Under the high FE_{NH3} and selectivity, the BTC/La-Co_3O_{4-x} presents a higher partial current density and yield rate for NH_3 (97.70 mA cm^{-2} for j_{NH3} and 31.24 mg h^{-1} mg$_{cat}^{-1}$ for Y_{NH3}) at −0.7 V vs. RHE, about 1.79/1.58 and 2.87/2.48 times higher than j_{NH3}/Y_{NH3} of La-Co_3O_{4-x} and Co_3O_4, respectively. The intrinsic activity of these catalysts is subsequently assessed by normalizing the electrochemically active surface area (ECSA; Figure S22). Remarkably, the ECSA-normalized current densities have the same trend as the unnormalized LSV curves, where BTC/La-Co_3O_{4-x} exhibits the highest activity among the measured potential range,

indicating the distinguished intrinsic activity for eNO_3RR. This performance is notably superior to state-of-the-art catalysts reported in the literature, particularly regarding the yield rate for NH_3 (Figure 3F; Table S3). In fact, its NH_3 synthesis rate ranks among the most NH_3-synthesizing electrocatalysts, which is promising for large-scale NH_3 electrosynthesis.

To validate the fast $*NO_3$-to-$*NO_2$ activity after La doping and the suppressed HER due to BTC ligands, we conduct a comparative electrochemical assessment in the electrolytes containing 0.05 M NO_2^- or 0.05 M NO_3^-, respectively. As shown in Figures S23 and S24, the higher current density and yield rate of NH_3 in electrochemical NO_2^- reduction reaction (eNO_2RR) highlight the much easier reaction kinetics than eNO_3RR. Accordingly, there is a big gap between the FE_{NH3} for eNO_2RR and eNO_3RR of pure Co_3O_4, which suggests the reaction barrier during the conversion from $*NO_3$ to $*NO_2$, that is, leading to the high yield rate of NO_2^- as proved in Figure 3B. On the contrary, introducing La atoms into the Co_3O_4 lattice distinctly narrows this difference. This effect is caused by the generated O_v implementing abundant electron supply and faster electron transfer rate, overcoming the block during the $*NO_3$-to-$*NO_2$ process. It is important to note that the FEs depicted in Figure S24 exhibit a distinctive volcano-shaped profile. However, for BTC/La-Co_3O_{4-x}, the difference between eNO_2RR and eNO_3RR is minimal, and the volcano shape is comparatively subdued, particularly at more negative potentials, suggesting the suppressed HER. Consequently, it can be deduced that the high-rate eNO_3RR performance observed in BTC/La-Co_3O_{4-x} is attributed to the coexistence of the synergistically generated O_v and carboxylate groups in BTC ligands, in which the former catalyzes the reduction from $*NO_3$ to $*NO_2$ and the latter suppresses the competing HER, thereby contributing to the tandem catalysis of nitrate. In practical wastewater treatment, where polluted nitrate concentrations can vary from 0.88 mM to 1.95 M,[54] it is crucial to assess the performance of the electrolyte with different nitrate concentrations ($[NO_3^-]$). As displayed in Figure S25, the Y_{NH3} climbs with the increasing $[NO_3^-]$ (5–500 mM) at −0.3 V vs. RHE. Remarkably, the FE_{NH3} exceeds 70% at all the concentrations and 90% at the $[NO_3^-]$ of 10–500 mM, indicating the promising potential of BTC/La-Co_3O_{4-x} in eNO_3RR for environmental applications. The slight reduction of FE_{NH3} when the $[NO_3^-]$ surpasses 50 mM is more likely because of the deactivation of the active sites due to the sluggish transfer of generated NH_3.[18,55] Additionally, the ^1H nuclear magnetic resonance (NMR) analysis is undertaken to confirm the origin of the nitrogen incorporated in the produced NH_3 (Figure S26). The absence of a peak in the ^1H NMR spectra prior to the nitrate reduction reaction is changed to the characteristic splitting modes in the spectra that measure the standard $^{14}NH_4^+$ or $^{15}NH_4^+$ electrolyte after eNO_3RR, proving all nitrogen in the generated NH_3 comes from ^{15}N isotope-labeled $^{15}NO_3^-$ or ^{14}N isotope-labeled $^{14}NO_3^-$. Moreover, the concentrations of detected $^{15}NH_4^+$ of all the samples are closely similar to that measured by the UV-visible (UV-vis) method, which suggests the accuracy of the data obtained in this work. To estimate the electrochemical durability of BTC/La-Co_3O_{4-x} for eNO_3RR, we perform consecutive cycling tests at −0.3 V vs. RHE (Figure 3G). After eight cycles, both the yield rates and FEs of NH_3 product are well preserved, indicating excellent stability with a stable FE_{NH3} exceeding 95% and Y_{NH3} beyond 5.50 mg h^{-1} mg_{cat}^{-1} over the cycles. The morphology and valence states of BTC/La-Co_3O_{4-x} after the stability test also have no significant change (Figures S27 and S28).

Mechanism study and computational insights into the eNO_3RR on BTC/La-Co_3O_{4-x} NPs

To gain a comprehensive understanding of the underlying mechanism driving the enhanced eNO_3RR activity of BTC/La-Co_3O_{4-x} NPs, we first perform DFT

calculations to investigate the interaction between BTC ligands and water molecules. As delineated by the electrostatic potential (ESP) mapping (Figure 4A), a positive potential envelopes the H atoms in water, while a negative potential surrounds the O atoms in the COO^- group of BTC ligands. This distribution indicates the inherent electrostatic interaction between them, constituting the formation of H-bonds (H … O–H). Subsequently, the binding energy of water molecules to BTC ligands was computed to be −0.367 eV, thereby affirming the robustness of the H-bonding interaction.[56] Furthermore, the MD simulations were undertaken to explore the molecular behavior, including H_2O and NO_3^-, at the side of the interface from the electrolyte (Figures 4C and 4D). It could be found that water molecules are bonded with neighbor COO^- by H-bonds in the simulated results (the enlarged photo in BTC/La-Co_3O_{4-x}). Notably, the presence of electrostatic mutual repulsion between the negatively charged COO^- and NO_3^- ions precludes the formation of H-bonds between them,[57] whereas this ensures enough NO_3^- could be adsorbed by active sites for eNO_3RR. After a simulation duration of 100 ns, a comparative analysis is made between the near-surface molecule behaviors of BTC/La-Co_3O_{4-x}, modified by BTC ligands, and the pure Co_3O_4 catalyst. These results, as depicted in the concentration profile of Figure 4E, unveil a relatively low concentration of ions in the near-surface region of BTC/La-Co_3O_{4-x}, validating the constrained water activity due to the formation of H-bonds between water and COO^- ligands. Besides, the results are the same when we place BTC/La-Co_3O_{4-x} and Co_3O_4 in 1.0 M KOH solution without NO_3^-, of which a higher concentration of H_2O is observed at the interface of Co_3O_4 (Figure S29). These computational findings collectively expound upon the reasons behind the limited proton accessibility of BTC/La-Co_3O_{4-x} and its consequent lower FE_{H2} during nitrate reduction. The limitation of proton accessibility influences the selectivity between H^+ and NO_3^- for an active site, in which NO_3^- is preferentially adsorbed instead of H^+, promoting the kinetics of eNO_3RR and suppressing HER. The MD simulations provide invaluable insights into the role of H-bonds and electrostatic interactions in shaping the behavior of these catalysts in nitrate reduction processes. Since BTC has three COO^- groups, terephthalic acid (TPA) with two COO^- groups is combined with La-Co_3O_{4-x} to study the eNO_3RR performance (Figure S30). As anticipated, the current density observed with TPA/La-Co_3O_{4-x} exhibits a marginal reduction compared to that of BTC/La-Co_3O_{4-x} and achieves a higher FE_{NH3} of 97.84% at −0.4 V vs. RHE and Y_{NH3} of 23.73 mg h^{-1} mg_{cat}^{-1} at −0.7 V vs. RHE. The superior but lower performance of TPA/La-Co_3O_{4-x} compared to BTC/La-Co_3O_{4-x} suggests the pivotal role of carboxylic groups in the organic ligands as the efficient functional component enhancing the eNO_3RR rate. Concurrently, the greater number of carboxylic groups in BTC leads to a more remarkable eNO_3RR performance than TPA. To offer a clearer understanding of the diffusion behaviors of NO_3^- and H_2O, a schematic is depicted in Figure 4F. During the eNO_3RR process, the La-doped Co_3O_4 surface demonstrates a propensity for facile adsorption of NO_3^- ions through interaction with O_v sites. Conversely, H_2O molecules encounter hindrance due to the presence of COO^- ligands on BTC, which gives rise to the formation of H-bonds. The confined transfer channels for H_2O limit the accessibility of protons to active sites; meanwhile, the electrostatic mutual repulsion between COO^- and NO_3^- further ensures the preferential adsorption of NO_3^- ions. After that, the water bonded by H-bonds supplies protons to intermediates adsorbed on active sites and motivates PCET steps in eNO_3RR, eventually generating NH_3. Therefore, this phenomenon decreases the competing HER and significantly promotes the selectivity of eNO_3RR.

After the simulation, we use the *in situ* thin-layer FTIR spectrum to track intermediate species within a thin electrolyte layer above the surface of catalysts during the

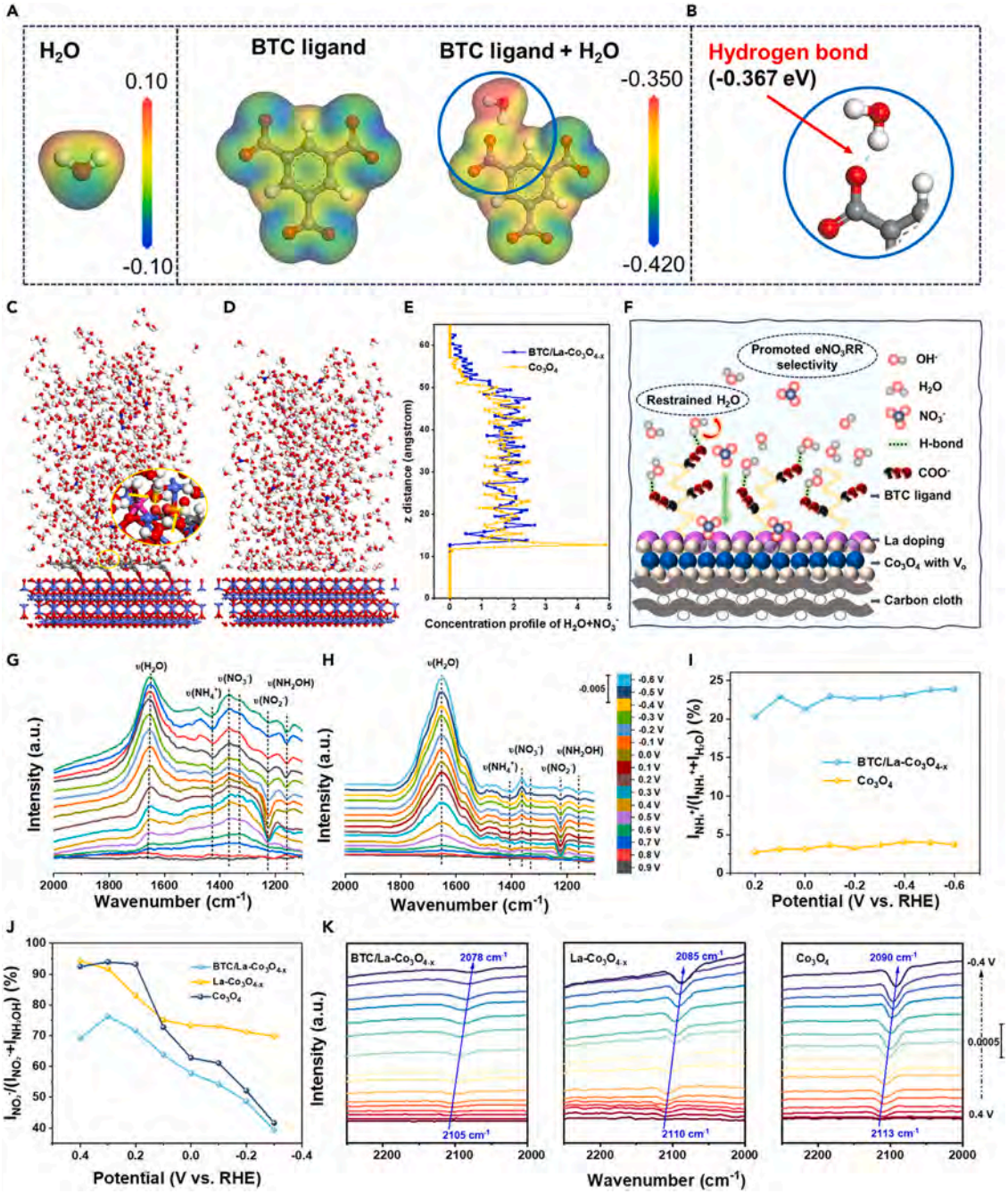

Figure 4. Simulating calculations and electrochemical *in situ* FTIR spectra

(A) Electrostatic potential (ESP) mapping of H_2O, BTC ligand, and BTC ligand with H_2O molecules.

(B) Calculated binding energy of the H-bond between water and BTC molecule.

(C) Molecular dynamics simulation of BTC/La-Co_3O_{4-x} in 1.0 M KOH solution + 10 mM KNO_3.

(D) Molecular dynamics simulation of Co_3O_4 in 1.0 M KOH solution + 10 mM KNO_3.

(E) Distribution of H_2O + NO_3^- along the z axis electrode distance based on molecular dynamics simulation.

(F) The schematic diffusion behaviors of NO_3^- and H_2O on the surface of BTC/La-Co_3O_{4-x} electrode.

(G) Electrochemical thin-layer *in situ* FTIR spectra of BTC/La-Co_3O_{4-x} during eNO_3RR.

(H) Electrochemical thin-layer *in situ* FTIR spectra of Co_3O_4 during eNO_3RR.

(I) Calculated $I_{NH4+}/(I_{NH4+} + I_{H2O})$ ratios from *in situ* FTIR spectra.

(J) Calculated $I_{NO2-}/(I_{NO2-} + I_{NH2OH})$ ratios from *in situ* FTIR spectra.

(K) Electrochemical *in situ* ATR-SEIRAS spectra of BTC/La-Co_3O_{4-x}, La-Co_3O_{4-x}, and Co_3O_4, respectively.

reaction, which will bring in-depth insights into eNO_3RR mechanisms. Herein, a reference spectrum (R_{ref}) is established at a potential of 0.9 V, and working spectra (R_S) are then obtained along with the potentials increased at an interval of 0.1 V. The acquired FTIR spectra are displayed as relative changes in the reflectance, denoted as $\Delta R/R = (R_S - R_{ref})/R_{ref.}$ [51] Consequently, the peaks ascending in FTIR spectra mean the consumption of reactants, including NO_3^- and H_2O, while the downward peaks correspond to the emergence of intermediates and resultant products, such as NO_2^-. Accordingly, in Figures 4G, 4H, and S31, six distinct absorption bands stand out, centered at 1,157, 1,226, 1,326, 1,365, 1,427, and 1,650 cm^{-1}, respectively. Firstly, the upward bands located at 1,326 and 1,365 cm^{-1} are attributed to the N–O asymmetric stretching vibration of NO_3^-, which occurs obviously after the potential surpasses 0.3 V, close to the onset potential in Figure 3A, indicating the beginning of nitrate reduction.[58] Besides, three downward bands around 1,157, 1,226, and 1,427 cm^{-1} are ascribed to –N–O– stretching vibration of intermediate hydroxylamine (NH_2OH), N–O antisymmetric stretching vibration of NO_2^- and N–H bending mode of NH_4^+ species, respectively,[18,59,60] demonstrating the generated NO_2^- from reducing NO_3^- and the following reduction by-products of NH_2OH, eventually leading to the final products of NH_3. Finally, the upward FTIR bands centered at 1,650 cm^{-1} are related to water electrolysis, a phenomenon responsible for hydrogeneration leading to NH_3 evolution after deoxygenation. The evident decreased water activity in BTC/La-Co_3O_{4-x} illustrates the existence of H-bonds. To better understand the relationship between different reactants and products, we calculate the $I_{NH4+}/(I_{NH4+} + I_{H2O})$ and $I_{NO2-}/(I_{NO2-} + I_{NO2-+NH2OH})$ ratios ("I" means intensity) from *in situ* FTIR spectra. As is known, both HER and eNO_3RR processes necessitate *H originating from water electrolysis; thereby, the high I_{H2O} accelerates the hydrogeneration essential for eNO_3RR and expedites hydrogen evolution. Drawing from the earlier discussion, it is clear that BTC ligands restrain water activity and suppress HER by forming H-bonding between H_2O molecules and COO^-. Therefore, the $I_{NH4+}/(I_{NH4+} + I_{H2O})$ ratio could provide support in clarifying the proportion of consumed *H in these two competing reactions and demonstrating the NH_3 selectivity of BTC/La-Co_3O_{4-x} and Co_3O_4 (Figure 4I; Table S4). It was found that the ratio of BTC/La-Co_3O_{4-x} is significantly higher than that of Co_3O_4, which suggests that much more *H is being used to generate NH_4^+ rather than H_2 during eNO_3RR, indicating the good NH_3 selectivity in BTC/La-Co_3O_{4-x} and also proving the advantageous role of organic BTC ligands in suppressing competing HER. Furthermore, it becomes apparent that the $\nu(NH_2OH)$ bands manifest after the formation of $\nu(NO_2^-)$ bands. This pattern indicates the gradually faster conversion from NO_2^- to NH_2OH through hydrodeoxidation, encompassing crucial steps such as the transition from NO_2^- to $*NO_2$ and the ensuing hydrogeneration process by increased applied potential. Therefore, the comparison in band intensity of NO_2^- relative to the collective intensity of NO_2^- and NH_2OH $[I_{NO2-}/(I_{NO2-} + I_{NH2OH})]$ serves as a visual indicator of the conversion rate from NO_2^- to NH_2OH via hydrodeoxidation. The various ratios of the samples exhibit a consistent declining trend as the applied potential increases in Figure 4J and Table S5. Interestingly, BTC/La-Co_3O_{4-x} and La-Co_3O_{4-x} have similar slopes, yet they are notably steeper when compared to Co_3O_4. This observation confirms the significant impact of La doping-induced O_v, proving the role in facilitating the gradual reduction from NO_2^- to the following products, such as NH_2OH. More importantly, the lowest ratios of BTC/La-Co_3O_{4-x} suggest the best eNO_3RR performance among the samples. In Figure 4K, the ATR-SEIRAS spectra, which have bands ranging from 2,078 to 2,113 cm^{-1}, can be observed, representing original metal–H-bonds influenced by the Stark effect.[61–64] Interestingly, an increased trend of metal–H (Co–H)-bonding emerges as the order of BTC/La-Co_3O_{4-x}, La-Co_3O_{4-x}, and Co_3O_4 at the same potential. This effect points to much

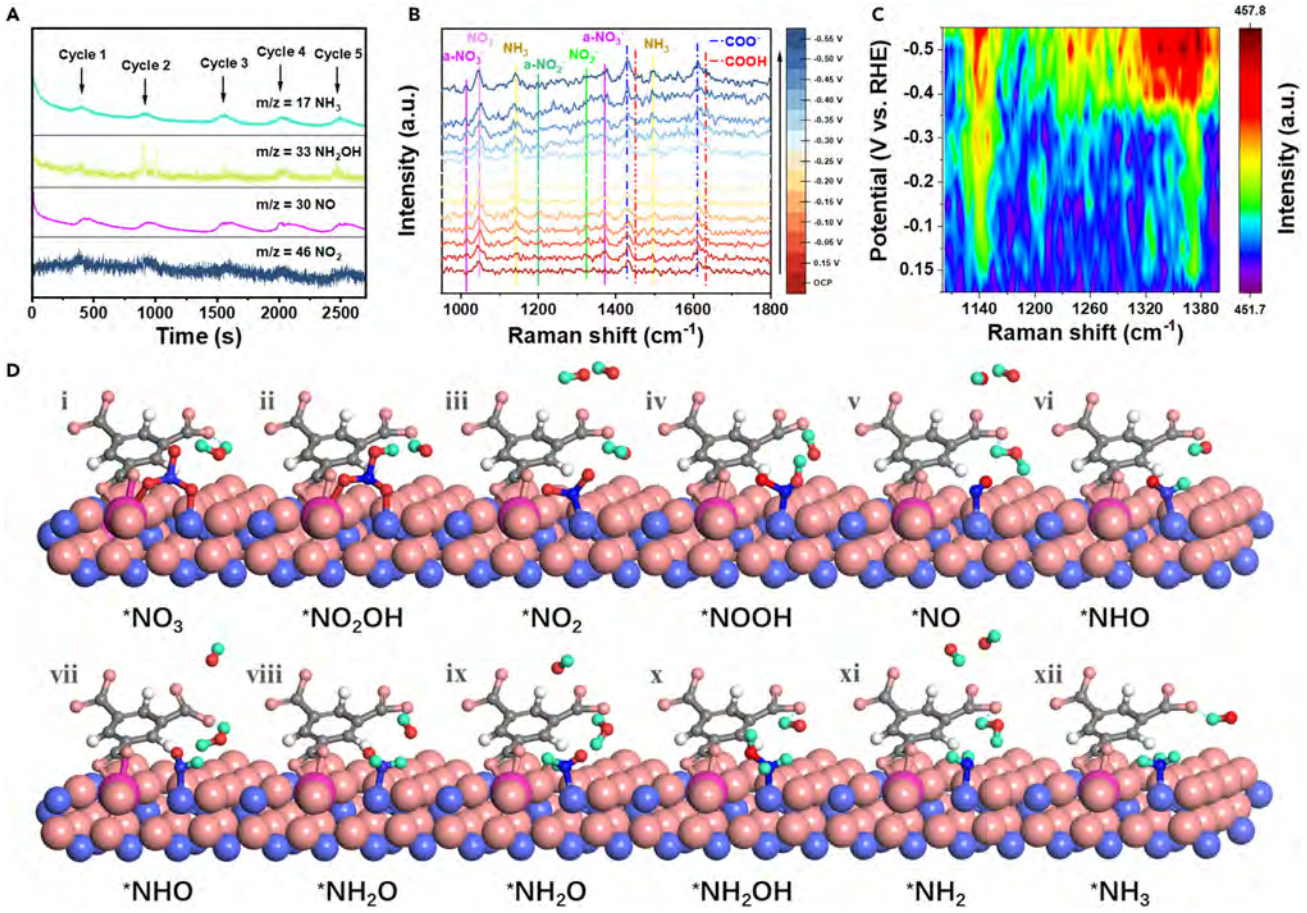

Figure 5. Reaction pathway during eNO_3RR over BTC/La-Co_3O_{4-x}

(A) Differential electrochemical mass spectrometry (DEMS) measurements of eNO_3RR on BTC/La-Co_3O_{4-x}.

(B) *In situ* Raman spectra of BTC/La-Co_3O_{4-x} during eNO_3RR at different potentials in a mixed solution (0.1 M KOH + 50 mM KNO_3).

(C) Corresponding contour plots from 1,100 cm^{-1} to 1,400 cm^{-1} in (B).

(D) The proposed structural models represent various intermediates and proton transfer mediators on BTC/La-Co_3O_4 during the pathway of eNO_3RR. The red, dark blue, and green balls represent O, N, and H atoms that participate in the eNO_3RR.

less *H adsorption on the surface of BTC/La-Co_3O_{4-x}, which means more NO_3^- adsorbed on active sites and the fast consumption of *H. Moreover, the higher wavenumbers associated with Co–H-bonds in Co_3O_4 validate their enhanced *H-bonding capacity.[65] According to the analysis of *in situ* FTIR measurement, it can be concluded that the coexistence of induced O_v and COO^- organic ligands within BTC/La-Co_3O_{4-x} not only expedites the conversion of *NO_3^--*NO_2-NH_2OH but also suppresses the competitive HER process, limiting proton accessibility. This interplay culminates in a remarkable eNO_3RR performance characterized by high activity and selectivity.

To construct a comprehensive description of the reaction pathway of BTC/La-Co_3O_{4-x} during eNO_3RR, online DEMS was carried out for five subsequent LSV scan cycles (each cycle involves a scan from 0.5 to −0.7 V vs. RHE) to detect the intermediate species generated during the eNO_3RR. As depicted in Figure 5A, the mass-to-charge ratio (m/z) signals at 17, 30, 33, and 46 are detected via online DEMS, aligning with the identification of corresponding products: NH_3, NO, NH_2OH, and NO_2, respectively.[66] Notably, the detection of NH_2OH is of particular significance, as its presence is also tracked within the *in situ* FTIR spectra illustrated in

Figure 4G. This concurrent occurrence suggests the hydrodeoxidation pathway in this system follows the trajectory from $*NO_2$ to $*NH_2OH$. Furthermore, the investigation extends to *in situ* Raman spectra acquired from BTC/La-Co_3O_{4-x} in a solution containing NO_3^- (Figure 5B). Besides the Raman peaks associated with $–COO^-$ and –COOH functionalities, additional bands have been attributed to three distinct groups: NO_3^- vibrations (1,047 cm^{-1}) and adsorbed NO_3^- species (1,013 and 1,372 cm^{-1}), generated NO_2^- vibrations (1,324 cm^{-1}) and adsorbed NO_2^- species (1,198 cm^{-1}), and generated NH_3 vibrations (1,142 and 1,495 cm^{-1}).[67] To facilitate a more comprehensive understanding of these diverse intermediates, a corresponding contour plot ranging from 1,100 cm^{-1} to 1,400 cm^{-1} is depicted in Figure 5C, derived from the data showcased in Figure 5B. As anticipated, the bands associated with adsorbed NO_3^- and generated NH_3 appear after open-circuit potential (OCP), and their intensities gradually increase as the potential becomes more negative, indicating the more active eNO_3RR on BTC/La-Co_3O_{4-x}. More importantly, the bands for producing NO_2 are detected from the potential range from 0.15 to −0.15 V vs. RHE, consistent with the experimental results, but they disappear upon the appearance of adsorbed NO_2^- signals, which are discovered from −0.10 to −0.25 V vs. RHE, suggesting the gradually increasing capacity for adsorbing dissociative NO_2^- ions over BTC/La-Co_3O_{4-x}. Furthermore, the adsorbed NO_2^- band vanishes after the potential drops below −0.25 V vs. RHE, coinciding with a conspicuous enhancement in the Raman peak corresponding to NH_3. These observations validate the outstanding capacity of BTC/La-Co_3O_{4-x} to convert $*NO_3$ to $*NO_2$ to NH_3, underscoring its remarkable efficacy in facilitating the eNO_3RR process. Incorporating the insights garnered from DEMS and *in situ* Raman studies, we propose the possible eNO_3RR pathway and calculate the Gibbs free energy of each intermediate on BTC/La-Co_3O_{4-x} and the counterparts at different pH values by DFT (Figures 5D and S32–S35). In addition to the adsorption and desorption of NO_3^- and NH_3, respectively, the pathway involves a total of nine PCET steps during eNO_3RR, including the hydrodeoxidation process of $*NO_3$-$*NO_2OH$-$*NO_2$-*NOOH-*NO, as well as the hydrogenation procedures of *NO-*NHO-$*NH_2O$-$*NH_2OH$-$*NH_2$-$*NH_3$. As shown in Figure S32, the initial upward trend (0.25 eV) from NO_3^- to $*NO_3$ suggests an energetically unfavorable reaction of adsorbing NO_3^- over Co_3O_4, whereas it converts to downward trend (−0.33 eV for La-Co_3O_{4-x} and −0.48 eV for BTC/La-Co_3O_{4-x}) upon doping La atoms, indicating the easier adsorption of NO_3^- on the O_v site in La-Co_3O_{4-x}, which are also proved by the much more favorable NO_3^- adsorption energy on the O_v site compared to the Co site of La-Co_3O_{4-x} (Figure S36). The projected density of states (PDOS) clearly demonstrates the stronger hybridization between the O 2p orbital in NO_3^- and the 3d orbital of the Co atom in BTC/La-Co_3O_{4-x} (Figure S37). In the meantime, in both acidic and alkaline environments (pH values are 0 and 14, respectively), La-Co_3O_{4-x} and BTC/La-Co_3O_{4-x} exhibit a reduced uphill free energy change ($*NO_3$-$*NO_2OH$) in the next PCET reaction, coupled with a higher NO_2^- desorption capacity. The enhanced affinity of $*NO_2^-$ species prevents its desorption from generating NO_2^- by-product during reduction, significantly accelerating the conversion from $*NO_3$ to $*NO_2$. More importantly, the rate-determining step (RDS) is the conversion from *NO to *NHO. For BTC/La-Co_3O_{4-x}, the RDS exhibits a notably smaller energy barrier than that of La-Co_3O_{4-x} and Co_3O_4. This finding reflects the unique advantages of functional organic ligands compared to organic additives. That is, in addition to controlling proton accessibility, they can also regulate the local electronic environment around the active site to change the adsorption energy of various intermediates. Combining the above results, we proposed the structural models representing various intermediates and proton transfer mediators to give a straightforward understanding of the reaction pathway and PCET mechanisms

(Figure 5D). The key factor is the contribution of free H_2O molecules originating from the bulk electrolyte. These molecules undergo a sequence of interactions: initially, they engage in H-bonds with coordinatively unsaturated interfacial COO^- sites from organic ligands, effectively preventing the direct adsorption of H_2O on active sites and suppressing HER. In the subsequent step (ii), an H atom from the bonded H_2O joins with an O atom from $*NO_3$, facilitated by the provision of electrons from generated O_v, culminating in a complete PCET process. Simultaneously, the remaining –OH is released into the bulk electrolyte due to electrostatic repulsion forces between OH^- and COO^-, thereby ensuring enough COO^- that could bond with free H_2O. This sequence unfolds across each PCET step, effectively controlling the proton accessibility but not blocking them from participating in hydrogenation for the intermediates on active sites, giving a decisive contribution to the enhancement of eNO_3RR selectivity of BTC/La-Co_3O_{4-x}. Based on the results discussed above, we get a comprehensive description of the reaction pathway of the samples in this work. Herein, through a synergistic interplay of generated O_v resulting from La doping and COO^- groups in combined carboxylic-based organic ligands, the increment of eNO_3RR performance is achieved. The induced O_v acts as active sites for adsorbing NO_3^- while redistributing electrons and promoting the electron transfer to the PCET steps, making faster $*NO_3$-to-$*NO_2$ conversion and reducing the generated NO_2^- side-product. In tandem, the H-bonds formed between H_2O and COO^- lead to indirect proton accessibility to active sites in every PCET step, not only balancing the adsorption between *H and $*NO_3$ species but also lowering the energy barrier of RDS (*NO to *NHO), thus suppressing the competing HER and boosting both the selectivity and activity of eNO_3RR.

Conclusions

In summary, we designed an electrocatalyst of Co_3O_4 NPs modified with doped La atoms and COO^--based organic ligands. This innovative catalyst design has elucidated the significant synergistic effect of induced oxygen vacancies due to La doping and functionalized COO^- organic ligands on facilitating the nitrate adsorption, confining the water activity, and regulating the PCET steps in nitrate reduction. This BTC/La-Co_3O_{4-x} electrocatalyst exhibited high activity and selectivity during eNO_3RR, achieving an FE as high as 99.41% with an ammonia yield rate of 5.62 mg h^{-1} mg_{cat}^{-1} at −0.3 V vs. RHE. Notably, the catalyst sustains NH_3 production with >90% FE within a wide potential window (400 mV, from −0.3 to −0.7 V vs. RHE), which is top ranked among the electrocatalysts for eNO_3RR so far. The proposed reaction mechanism combines the results of *in situ* FTIR, *in situ* Raman, MD simulations, and DFT calculations. In detail, La doping provides abundant active sites (oxygen vacancies) for adsorbing NO_3^- and significantly lowers the energy barrier of $*NO_3$-to-$*NO_2$ steps, which are beneficial from electron redistribution. Also, the COO^- can form H-bonds with free water, thereby confining the water activity and leading to the controlled proton accessibility to active sites and regulated hydrogenation PCET steps, which plays a decisive contribution to the enhancement of selectivity of eNO_3RR. This work provides a rational strategy based on carboxylic organic ligands for a high ammonia production rate. It can contribute to subsequent catalyst optimization and scale-up for applications across diverse electrochemical techniques, particularly those where the HER poses a competing challenge, such as CO_2 reduction.

EXPERIMENTAL PROCEDURES

Resource availability

Lead contact

Requests for further information and resources should be directed to and will be fulfilled by the lead contact, Prof. Johnny C. Ho (johnnyho@cityu.edu.hk).

Materials availability

All catalysts generated in this study will be made available upon request, but we may require a payment and/or a completed materials transfer agreement.

Data and code availability

All data related to this study included in the article and supplemental information will be provided by the lead contact, Prof. Johnny C. Ho (johnnyho@cityu.edu.hk), upon reasonable request.

Preparation of Co_3O_4 NPs

The Co_3O_4 NPs were prepared via a facile coprecipitation method. Typically, 0.25 mM cobalt nitrate hexahydrate ($Co(NO_3)_2 \cdot 6H_2O$, Sigma-Aldrich) was dissolved into 25 mL of deionized (DI) water. After vigorous stirring for 1 h, 25 mL of 0.375 M NaOH solution was slowly dropwise into the $Co(NO_3)_2$ precursor solution. After further stirring for 2 h, the precipitate was washed with DI water and ethyl alcohol several times and collected by centrifugation, followed by vacuum drying at 60°C overnight. The resulting cakes were crushed into fine powder in a mortar and then calcined in air at 500°C for 5 h.

Preparation of La_y-Co_3O_{4-x}, where y represents the atom % of La

For La_y-Co_3O_{4-x}, 5, 15, and 25 mg of $La(NO_3)_3 \cdot 6H_2O$ (Sigma-Aldrich) were added into the $Co(NO_3)_2$ precursor solution, respectively. The subsequent procedures were the same as preparing Co_3O_4 NPs. The atom % of La were determined to be 3.02, 6.29, and 9.11 atom % by inductively coupled plasma emission spectrometry (ICP-OES), which were named as La_3-Co_3O_{4-x}, La_6-Co_3O_{4-x} and La_9-Co_3O_{4-x}, respectively.

Preparation of BTC/La-Co_3O_{4-x}

Herein, La_9-Co_3O_{4-x} was chosen as a sample for combining with BTC ligands, abbreviated here as La-Co_3O_{4-x}. In detail, 5 mg of H_3BTC (Sigma-Aldrich) and 50 mg of La-Co_3O_{4-x} were mixed with 20 mL of dimethylformamide (DMF, Sigma-Aldrich), followed by stirring for 2 h. Finally, the precipitate was washed and centrifuged several times with fresh DMF, ethyl alcohol, and DI water, followed by vacuum drying at 60°C overnight.

Characterization

Scanning electron microscopy (SEM; FEI Quanta 450 FESEM), transmission electron microscopy (TEM; Tecnai G2 20), HRTEM (Tecnai G2 20), and SAED were used to observe the micromorphology and elemental distribution of the catalysts. XRD patterns were collected using a Bruker D8 Advance powder diffractometer to investigate the phase structures. XPS analyses using a Thermo Fisher ESCALAB XI+ system with an Al-Kα X-ray source (hν = 1,486.6 eV) was used to determine the elemental composition and valence state. All XPS spectra were corrected with a C 1s spectral line of 284.8 eV. ICP-OES (Agilent 730es) was carried out to determine the chemical composition of the catalysts. The electrolytes after electro-reduction were analyzed by UV-vis spectroscopy (Hitachi UH4150 UV-vis-NIR Spectrophotometer). To determine the origin of the ammonia produced, isotope labeling experiments were conducted on a Bruker 400MHz AVANCE III Nuclear Magnetic Resonance System (NMR-400). Zeta potential was determined by SurPASS 3 from Anton Paar in Austria in an aqueous solution (pH = 7). FTIR spectroscopy was recorded on a PerkinElmer FTIR Spectrometer. The XANES and the EXAFS analyses were investigated using the Singapore Synchrotron Light Source (SSLS) at the National University of Singapore. The sample was measured in transmission mode using La_2O_3 as a reference sample. All X-ray absorption fine structure (XAFS) spectra were processed using the IFEFFIT package. Data reduction, data analysis,

and EXAFS fitting were conducted using the Athena and Artemis programs from the Demeter data analysis packages, which utilize the FEFF6 program for EXAFS data fitting.[68,69] The energy calibration of the sample was conducted through standard, which as a reference was simultaneously measured. A linear function was subtracted from the pre-edge region, then the edge jump was normalized using Athena software. The χ(k) data were isolated by subtracting a smooth, third-order polynomial approximating the absorption background of an isolated atom. The k^3-weighted χ(k) data were Fourier transformed after applying a HanFeng window function (Δk = 1.0). For EXAFS modeling, the global amplitude EXAFS (*CN*, *R*, σ^2, and ΔE_0) was obtained by nonlinear fitting, with least-squares refinement, of the EXAFS equation to the Fourier transformed data in R space, using Artemis software, the amplitude reduction factor S_0^2 value (0.900) was set in the EXAFS analysis to determine the coordination numbers (CNs) in the La-O and La-Co scattering path in sample. For wavelet transform analysis, the χ(k) exported from Athena was imported into the Hama Fortran code. The parameters were listed as follows: R range, 0–6 Å; k range, 0–16.0 Å-1; k weight, 3; and Morlet function with κ = 8, σ = 1 was used as the mother wavelet to provide the overall distribution.[70]

Electrochemical characterization

All the electrochemical measurements were carried out with an electrochemical workstation of Gamry G300 potential station at room temperature in an H-type electrolytic cell separated by a Nafion 117 membrane (DuPont). The anode chamber contained 50 mL of 0.1 M KOH electrolyte, while the cathode chamber contained 50 mL of 0.1 M KOH electrolyte with 0.05 M NO_3^-. High-purity argon gas was bubbled into the cathodic chamber during electro-reduction to prevent possible side-competitive reactions such as the nitrogen reduction reaction (NRR). To prepare working electrodes, 5 mg of catalysts was dispersed in 960 μL of solution with DI water and ethanol (3:1, v/v), followed by the addition of 40 μL of Nafion solution. After sonicating for 1 h to form well-mixed inks, 50 μL of ink was drop-casted on carbon cloth (CC; 1 × 1 cm) to attain a working electrode with a loading of 0.25 mg cm^{-2}. In the three-electrode system, the catalysts on CC were used as working electrodes and a piece of Pt and Ag/AgCl (saturated KCl electrolyte) represented the counter and reference electrodes, respectively.

The LSV curves were recorded by a scan rate of 5 mV s^{-1}. Electrochemical impedance spectroscopy (EIS) was obtained in the frequency range from 0.01 Hz to 100 kHz upon an alternating current (AC) voltage amplitude of 5 mV. The cyclic voltammetry curves were measured in a potential window where no Faradaic process occurred at different scanning rates (10–80 mV s^{-1}) to determine the electrochemical double-layer capacitance (C_{dl}). For eNO_3RR experiments, potentiostatic tests were conducted for 1 h at different potentials with a magnetic stirring rate of 300 rpm. To ensure data accuracy, each catalyst was prepared for three samples for testing three times to get the error bar. All potentials were adjusted to the RHE using Equation 4:

$$E\,(\text{vs. RHE}) = E\,(\text{vs. Ag/AgCl}) + 0.059 \times \text{pH} + 0.197\ \text{V} \qquad \text{(Equation 4)}$$

Electrochemical *in situ* Raman spectroscopy analysis

In situ Raman spectra were collected on the WITec alpha300 R Raman System with an excitation wavelength of 532 nm. The working electrodes were cut to a plate shape with a diameter of 1 cm and put into the Raman cell with a quartz window. A platinum wire and Ag/AgCl served as the counter and reference electrodes, respectively. The Raman spectra were obtained at different potentials under control by an electrochemical workstation in the electrolyte of Ar-saturated 0.1 M KOH with 0.05 M KNO_3. Each spectrum was an average of five continuously acquired spectra with a collection time of 30 s.

Electrochemical *in situ* FTIR reflection analysis

Electrochemical thin-layer *in situ* FTIR reflection spectroscopy was performed on a Nicolet iS50 spectrometer equipped with an mercury-cadmium-telluride (MCT) detector at different potentials controlled by an electrochemical workstation CHI760E. In detail, the catalyst ink was loaded on a glassy carbon electrode as a working electrode and pressed vertically on the CaF_2 window plate. There was a thin electrolyte (0.1 M KOH with 0.05 M KNO_3) layer with a thickness of about 10 μm between the glassy carbon electrode and CaF_2 plate. Ar was used to purge the dissolved O_2 and N_2 from the electrolyte. A platinum foil and an Ag/AgCl electrode were used as the counter and reference electrodes, respectively. The spectra were collected at different potentials (from 0.9 to −0.6 V vs. RHE) with an interval of 0.1 V. Reference spectra were collected at 0.9 V vs. RHE. Attenuated total reflection surface-enhanced infrared absorption spectroscopy (ATR-SEIRAS) was also performed using a Nicolet iS50 spectrometer. Different from thin-layer FTIR experiments, the catalyst ink was dropped on a silicon crystal chemically deposited by a thin gold film. The incoming infrared beam has an angle of ca. 65° with the normal electrode surface. The spectra were collected at different potentials (from 0.4 to −0.4 V vs. RHE) with an interval of 0.05 V.

Online DEMS measurements

The online DEMS system consists of an electrochemical workstation and a mass spectrometer. The sampling probe of the mass spectrometer faces the working electrode of the electrochemical cell. Online DEMS measurement was performed on a homemade electrochemical cell with an electrolyte of 0.1 M KOH and 0.05 M NO_3^- equipped with a peristaltic pump. Ar was constantly bubbled into the electrolyte before and during the DEMS measurements. The system was controlled by an electrochemical workstation (CHI760E) with three electrodes: a glassy carbon electrode coated with BTC/La-Co_3O_{4-x} NPs electrocatalysts, Pt wire, and saturated Ag/AgCl electrode were used as the working electrode, the counter electrode, and the reference electrode, respectively. The glassy carbon electrode was inserted from the bottom of the electrochemical cell. During the eNO_3RR, the electrolyte flows into the thin layer in front of the electrode. Then, it flows into the detection cell through the capillaries, where the volatile chemicals can reach the detector through the Teflon membrane. LSV technology was employed from 0.5 to −0.7 V vs. RHE at a scan rate of 2 mV s^{-1} for five cycles.

Determination of products

NH_3

The concentration of NH_3 was quantified by the indophenol blue method.[71] The electrolytes after electrolysis for 1 h were first removed from the electrochemical cell and diluted to the detection range. Then 2 mL of diluted electrolyte was taken out into a test tube, followed by adding 2 mL of solution A, which was prepared by mixing 5.0 wt % salicylic acid ($C_7H_6O_3$) and 5.0 wt % sodium citrates ($C_6H_5Na_3O_7 \cdot 2H_2O$) into 1.0 M NaOH solution. Then, 1 mL of solution B (diluted NaClO solution with a concentration of 0.05 M) was added to the above solution, followed by adding 0.2 mL of solution C (1.0 wt % sodium nitroferricyanide, $Na_2[Fe(NO)(CN)_5] \cdot 2H_2O$). The test tube was placed on the test tube rack and stood for 2 h in a dark place under ambient conditions. The absorption spectrum of the solution was measured by UV-vis spectrophotometry, then the absorbance value was collected at a wavelength of 655 nm. The concentration-absorbance calibration curve of NH_3 was plotted by measuring the absorbance values of a series of standard NH_4Cl solutions of known concentration dissolved in 0.1 M KOH.

NO_2^-

The concentration of NO_2 was quantified using the Griess method.[72] After electrolysis for 1 h, the electrolytes were first removed from the electrochemical cell and diluted to the detection range. A 5-mL diluted electrolyte was removed into a test tube, and 0.1 mL of color reagent was added. The color agent was prepared as follows: 50 mL of DI water and 10 mL of phosphoric acid were mixed together, followed by adding 4.0 g of *p*-aminobenzenesulfonamide and 0.2 g of N-(1-naphthyl)-ethylenediamine dihydrochloride. The mixture was then poured into a 100-mL volumetric flask and diluted to the calibration tail. The test tubes were then shaken, put in a test tube rack, stood for 20 min under ambient conditions, the solution's absorption spectrum measured with a UV-vis spectrophotometer, and the absorbance value collected at a wavelength of 540 nm. The concentration-absorbance calibration curve was plotted by measuring the absorbance values of a series of standard KNO_2 solutions of known concentration dissolved in 0.1 M KOH.

N_2H_4

The concentration of N_2H_4 was quantified by Watt and Chrisp's method.[73] Two milliliters of diluted electrolyte was taken out into a test tube, followed by adding 2 mL of color reagent, which contains 5.99 g of p-(dimethylamino)benzaldehyde, 30 mL of concentrated HCl, and 300 mL of ethanol The test tubes were then shaken, put in a test tube rack, stood for 30 min under ambient conditions, the solution's absorption spectrum measured with a UV-vis spectrophotometer, and the absorbance value collected at a wavelength of 460 nm. The concentration-absorbance calibration curve was plotted by measuring the absorbance values of a series of concentrations known as standard N_2H_4 solutions dissolved in 0.1 M KOH.

Isotope labeling experiment

The isotope labeling experiments were recorded by Bruker 400MHz AVANCE III Nuclear Magnetic Resonance System (NMR-400) using maleic acid ($C_4H_4O_4$) as the internal standard. The nitrate reduction experiments were the same as usual, other than replacing $K^{14}NO_3$ with $K^{15}NO_3$ (98.5 atom%) as the feeding N-source for the isotopic label. Specifically, the obtained electrolytic electrolyte containing $^{15}NH_4^+$-^{15}N was removed and adjusted to weak acid with 4 M H_2SO_4. A 10-mL solution was extracted into the test tube, and 4 mg of maleic acid was added. Subsequently, 0.5 mL of the above solution and 50 μL of D_2O were injected into a nuclear magnetic tube for NMR detection. As for the calibration curve, a series of $^{15}NH_4^+$-^{15}N solutions ($^{15}NH_4Cl$) with known concentrations were set up for NMR measurement. Since the $^{15}NH_4^+$-^{15}N concentration and the area ratio in the NMR spectra were positively correlated, the calibration was achieved using the peak area ratio between $^{15}NH_4^+$-^{15}N and maleic acid. Similarly, the amount of $^{14}NH_4^+$-^{14}N was quantified using the same method as above, where $^{14}KNO_3$ was used as the feeding N-source.

Computational formula

For nitrate electro-reduction, the yield rate was calculated by Equation 5:

$$NH_3 \text{ yield rate } \left(mg\, h^{-1}\, mg_{cat.}^{-1}\right) = \frac{CNH_3 \times V}{t \times m_{cat.}} \quad \text{(Equation 5)}$$

FEs of NH_3 and NO_2 were calculated by Equation 6 and 7:

$$FE_{NH_3}(\%) = \frac{8F \times CNH_3 \times V}{17 \times Q} \quad \text{(Equation 6)}$$

$$FE_{NO_2}(\%) = \frac{2F \times CNO_2 \times V}{46 \times Q} \quad \text{(Equation 7)}$$

where CNH_3 (mg mL^{-1}) and CNO_2 (mg mL^{-1}) are the measured concentrations of NH_3 and NO_2^-, respectively. V (mL) is the volume of the cathodic electrolyte, t (h) is the reduction time, $m_{cat.}$ (mg) is the mass loading of the catalyst on CC, F (96485 C mol^{-1}) is the Faraday constant, and Q (C) is the total charge passing the electrode.

Theoretical simulation

MD simulations

MD simulations were performed by using the Forcite Dynamic program. The simulation system was constructed by stacking a liquid phase onto the surface of BTC/La-Co_3O_{4-x} and Co_3O_4. The catalyst of La-Co_3O_{4-x} was not considered because we mainly used the MD simulations to prove the function of organic ligands. A typical unit cell model for cubic Co_3O_4 (8.0850 × 8.0850 × 8.0850) was used and then the (111) crystal plane was cleaved. The final model was a 4 × 4 unit cell of Co_3O_4 (111) surface with two layers. For BTC/La-Co_3O_{4-x}, an octahedral Co was substituted by the La atom, and an adjacent O atom was deleted to simulate the La-doped Co_3O_4 with oxygen vacancy. One H_3BTC molecule was bonded with an La atom. The liquid phase of KOH solution and KOH solution with NO_3^- were constructed by an amorphous cell module with COMPASSII force field and force field assigned charge calculation methods at 298.15 K. The liquid phase in a 2.6 nm × 2.6 nm × 2.6 nm contained 10 K^+, 10 OH^-, and 550 water molecules formed to simulate a 1.0 M KOH solution. Another 10 NO_3 was added to form a 1.0 M KOH solution with 10 mM NO_3. The geometry of the liquid/catalyst systems was first optimized by the Forcite module. The electrostatic interaction was calculated using the Ewald summation with an accuracy of 1.0 × 10^{-4} kcal mol^{-1}, and the van der Waals interaction was calculated using the atom-based summation.[74] Then, 100-ps MD runs were carried out under isothermal-isobaric (NPT) ensemble (298.15 K, 1 bar). Temperature and pressure were controlled by the Nose-Hoover thermostat and the Parrinello-Rahman barostat, respectively. Equations of motion were integrated by the leapfrog algorithm with a time step of 1 fs.

DFT calculations

All the computations were performed on the basis of the DFT using the Vienna ab initio Simulation Package (VASP) code.[75,76] The exchange-correlation function in the Perdew-Burke-Ernzerhof (PBE) form within a generalized gradient approximation (GGA) was used.[77,78] A typical unit cell model for cubic Co_3O_4 (8.0850 × 8.0850 × 8.0850) was used and then cleaved the (111) crystal plane. The final model was a 2 × 2 × 2 unit cell of Co_3O_4 (111) surface. For La-Co_3O_{4-x}, an octahedral Co was substituted by the La atom, and an adjacent O atom was deleted to simulate the La-doped Co_3O_4 with oxygen vacancy. For BTC/La-Co_3O_{4-x}, one H_3BTC molecule was bonded with the La atom in the La-Co_3O_{4-x} structure. Moreover, a vacuum spacing of ~15 Å was used to prevent spurious interaction between periodic images. During the calculation, the rock-bottom layer of the model is fixed. A cutoff energy of 450 eV for plain-wave basis sets was adopted, and the convergence criterion of the energy was set to be within 1.0 × 10^{-5} eV with forces on each atom less than 0.02 eV/Å. A 3 × 3 × 1 Monkhorst-Pack grid of k-points was selected to sample the Brillouin zone integration.

The NO_3^- reduction reaction on the surfaces of the catalysts was simulated by the following process:[79]

$$* + NO_3^-(aq) \rightarrow {}^*NO_3 + e^-$$

$$^{*}NO_3 + H_2O + e^- \rightarrow {}^{*}NO_2OH + OH^-$$

$$^{*}NO_2OH + e^- \rightarrow {}^{*}NO_2 + OH^-$$

$$^{*}NO_2 + H_2O + e^- \rightarrow {}^{*}NOOH + OH^-$$

$$^{*}NOOH + e^- \rightarrow {}^{*}NO + OH^-$$

$$^{*}NO + H_2O + e^- \rightarrow {}^{*}NOH + OH^-$$

$$^{*}NHO + H_2O + e^- \rightarrow {}^{*}NH_2O + OH^-$$

$$^{*}NH_2O + H_2O + e^- \rightarrow {}^{*}NH_2OH + OH^-$$

$$^{*}NH_2OH + e^- \rightarrow {}^{*}NH_2 + OH^-$$

$$^{*}NH_2 + H_2O + e^- \rightarrow {}^{*}NH_3 + OH^-$$

$$^{*}NH_3 \rightarrow * + NH_3\,(g)$$

where asterisks (*) represent the active sites. For each electrochemical step, the Gibbs free-energy changes (ΔG) for the eNO_3RR procedures were estimated according to Equation 8:[80]

$$\Delta G = \Delta E + \Delta ZPE - T\Delta S + \Delta G_U + \Delta G_{pH} \qquad \text{(Equation 8)}$$

where ΔE is the difference of energy calculated by DFT between the reactant and product, and ΔZPE is the change of zero-point energies, which could be evaluated by:

$$ZPE = N_a \sum_i \frac{h\nu_i}{2}$$

where N_a is the Avogadro number, h is the Planck constant, and ν_i represents the frequency. T is room temperature (298.15 K), and ΔS is the change of entropy obtained from the following equation:

$$S = R\sum_i \left\{ \frac{\left(\frac{h\nu_i}{k_B T}\right) exp\left(-\frac{h\nu_i}{k_B T}\right)}{\left[1 - exp\left(-\frac{h\nu_i}{k_B T}\right)\right]} - ln\left[1 - exp\left(-\frac{h\nu_i}{k_B T}\right)\right] \right\}$$

where R and k_B are the universal gas constant and the Boltzmann constant, respectively.

ΔG_U is the contribution of electrode potential, which can be calculated by $\Delta G_U = -eU$, where e is the number of electrons transferred, U is the applied potential measured against the standard hydrogen electrode, and U = 0 V is considered. ΔG_{pH} is the free-energy correction of pH, which can be calculated by $\Delta G_{pH} = -k_B T \times pH \times \ln 10$, and pH is set to be 0 and 14, respectively.

To calculate the Gibbs free energy of NO_3^-(aq) adsorption onto the electrode surface, the process could be divided into three steps, as follows:

$$NO_3^-(aq) + H^+ \rightarrow HNO_3(aq) \qquad \text{(Equation 9)}$$

$$HNO_3(aq) \rightarrow HNO_3(g) \qquad \text{(Equation 10)}$$

$$* + HNO_3(g) \rightarrow {}^*NO_3 + \frac{1}{2} H_2 \quad \text{(Equation 11)}$$

In Equation 9, the Gibbs free energy from NO_3^-(aq) to HNO_3(aq) formation is 0.317 eV. The Gibbs free energy for the vaporization of HNO_3(aq) was −0.074 eV. The Gibbs free energy of NO_3 adsorption on the active site (*NO_3) could be calculated as follows:

$$\Delta G_{ads}(*NO_3) = G(*NO_3) + \frac{1}{2} G_{gas}(H_2) - G(*) - G_{gas}(HNO_3)$$

Thus, the change of Gibbs free energy of NO_3 adsorption from the solution phase to the electrode surface for, i.e., * + NO_3^-(aq) → *NO_3 + e^- could be calculated as follows:

$$\Delta G(*NO_3) = \Delta G_{ads}(*NO_3) + 0.074\ eV + 0.317\ eV - \Delta G_{correct}$$

$\Delta G_{correct}$ is the correction of adsorption energy. The thermodynamic values (0.317 eV and 0.074 eV) are obtained from the CRC Handbook of Chemistry and Physics.[81]

SUPPLEMENTAL INFORMATION

Supplemental information can be found online at https://doi.org/10.1016/j.checat.2024.101024.

ACKNOWLEDGMENTS

This work was financially supported by the City University of Hong Kong (project nos. 9229138, 9678244, and 9231502).

AUTHOR CONTRIBUTIONS

D.C. and S.Z. contributed equally to this work. D.C., S.Z., D.Y., and Y.Z. carried out the synthesis, electrochemical measurements, and computational calculations. Q.Q., W.W., Y.M., and X.L. conducted part of the characterizations. D.C. and S.Z. participated in the analysis of the data. S.Y., T.Y., C.Z., and J.C.H. directed this work. All authors discussed and revised the manuscript.

DECLARATION OF INTERESTS

The authors declare no competing interests.

Received: January 13, 2024
Revised: May 4, 2024
Accepted: May 16, 2024
Published: June 11, 2024

REFERENCES

1. Valera-Medina, A., Xiao, H., Owen-Jones, M., David, W., and Bowen, P. (2018). Ammonia for power. Prog. Energy Combust. Sci. *69*, 63–102. https://doi.org/10.1016/j.pecs.2018.07.001.

2. Vojvodic, A., Medford, A.J., Studt, F., Abild-Pedersen, F., Khan, T.S., Bligaard, T., and Nørskov, J. (2014). Exploring the limits: A low-pressure, low-temperature Haber-Bosch process. Chem. Phys. Lett. *598*, 108–112. https://doi.org/10.1016/j.cplett.2014.03.003.

3. Humphreys, J., Lan, R., and Tao, S. (2021). Development and recent progress on ammonia synthesis catalysts for Haber-Bosch process. Adv. Energy and Sustain. Res. *2*, 2000043. https://doi.org/10.1002/aesr.202000043.

4. Jesudass, S.C., Surendran, S., Kim, J.Y., An, T.Y., Janani, G., Kim, T.H., Kim, J.K., and Sim, U. (2023). Pathways of the electrochemical nitrogen reduction reaction: from ammonia synthesis to metal-N_2 batteries. Electrochem. Energy Rev. *6*, 27. https://doi.org/10.1007/s41918-023-00186-6.

5. Jeong, Y., Janani, G., Kim, D., An, T.Y., Surendran, S., Lee, H., Moon, D.J., Kim, J.Y., Han, M.K., and Sim, U. (2023). Roles of Heterojunction and Cu Vacancies in the Au@Cu_{2-x}Se for the Enhancement of Electrochemical Nitrogen Reduction Performance. ACS Appl. Mater. Interfaces *15*, 52342–52357. https://doi.org/10.1021/acsami.3c07947.

6. Foster, S.L., Bakovic, S.I.P., Duda, R.D., Maheshwari, S., Milton, R.D., Minteer, S.D., Janik, M.J., Renner, J.N., and Greenlee, L.F. (2018). Catalysts for nitrogen reduction to ammonia. Nat. Catal. *1*, 490–500. https://doi.org/10.1038/s41929-018-0092-7.

7. Suryanto, B.H.R., Du, H.-L., Wang, D., Chen, J., Simonov, A.N., and MacFarlane, D.R. (2019). Challenges and prospects in the catalysis of electroreduction of nitrogen to ammonia. Nat.

Catal. *2*, 290–296. https://doi.org/10.1038/s41929-019-0252-4.

8. Shrimali, M., and Singh, K.P. (2001). New methods of nitrate removal from water. Environ. Pollut. *112*, 351–359. https://doi.org/10.1016/S0269-7491(00)00147-0.

9. Zeng, Y., Priest, C., Wang, G., and Wu, G. (2020). Restoring the nitrogen cycle by electrochemical reduction of nitrate: progress and prospects. Small Methods *4*, 2000672. https://doi.org/10.1002/smtd.202000672.

10. Gao, J., Shi, N., Li, Y., Jiang, B., Marhaba, T., and Zhang, W. (2022). Electrocatalytic upcycling of nitrate wastewater into an ammonia fertilizer via an electrified membrane. Environ. Sci. Technol. *56*, 11602–11613. https://doi.org/10.1021/acs.est.1c08442.

11. Zou, X., Chen, C., Wang, C., Zhang, Q., Yu, Z., Wu, H., Zhuo, C., and Zhang, T.C. (2021). Combining electrochemical nitrate reduction and anammox for treatment of nitrate-rich wastewater: A short review. Sci. Total Environ. *800*, 149645. https://doi.org/10.1016/j.scitotenv.2021.149645.

12. Garcia-Segura, S., Lanzarini-Lopes, M., Hristovski, K., and Westerhoff, P. (2018). Electrocatalytic reduction of nitrate: Fundamentals to full-scale water treatment applications. Appl. Catal., B *236*, 546–568. https://doi.org/10.1016/j.apcatb.2018.05.041.

13. Costa, G.F., Winkler, M., Mariano, T., Pinto, M.R., Messias, I., Souza, J.B., Neckel, I.T., Santos, M.F., Tormena, C.F., Singh, N., and Nagao, R. (2024). Identifying the active site of Cu/Cu_2O for electrocatalytic nitrate reduction reaction to ammonia. Chem Catal. *4*, 100850. https://doi.org/10.1016/j.checat.2023.100850.

14. Zhang, J., Chen, C., Zhang, R., Wang, X., Wei, Y., Sun, M., Liu, Z., Ge, R., Ma, M., and Tian, J. (2024). Size-induced d band center upshift of copper for efficient nitrate reduction to ammonia. J. Colloid Interface Sci. *658*, 934–942. https://doi.org/10.1016/j.jcis.2023.12.129.

15. Wu, Z.Y., Karamad, M., Yong, X., Huang, Q., Cullen, D.A., Zhu, P., Xia, C., Xiao, Q., Shakouri, M., Chen, F.Y., et al. (2021). Electrochemical ammonia synthesis via nitrate reduction on Fe single atom catalyst. Nat. Commun. *12*, 2870. https://doi.org/10.1038/s41467-021-23115-x.

16. Luo, H., Li, S., Wu, Z., Liu, Y., Luo, W., Li, W., Zhang, D., Chen, J., and Yang, J. (2023). Modulating the Active Hydrogen Adsorption on Fe-N Interface for Boosted Electrocatalytic Nitrate Reduction with Ultra-long Stability. Adv. Mater. *35*, 2304695. https://doi.org/10.1002/adma.202304695.

17. Fan, K., Xie, W., Li, J., Sun, Y., Xu, P., Tang, Y., Li, Z., and Shao, M. (2022). Active hydrogen boosts electrochemical nitrate reduction to ammonia. Nat. Commun. *13*, 7958. https://doi.org/10.1038/s41467-022-35664-w.

18. Zhang, N., Shang, J., Deng, X., Cai, L., Long, R., Xiong, Y., and Chai, Y. (2022). Governing Interlayer Strain in Bismuth Nanocrystals for Efficient Ammonia Electrosynthesis from Nitrate Reduction. ACS Nano *16*, 4795–4804. https://doi.org/10.1021/acsnano.2c00101.

19. Han, N., Wang, Y., Yang, H., Deng, J., Wu, J., Li, Y., and Li, Y. (2018). Ultrathin bismuth nanosheets from in situ topotactic transformation for selective electrocatalytic CO2 reduction to formate. Nat. Commun. *9*, 1320. https://doi.org/10.1038/s41467-018-03712-z.

20. Ren, Y., Yu, C., Tan, X., Huang, H., Wei, Q., and Qiu, J. (2021). Strategies to suppress hydrogen evolution for highly selective electrocatalytic nitrogen reduction: challenges and perspectives. Energy Environ. Sci. *14*, 1176–1193. https://doi.org/10.1039/D0EE03596C.

21. Peng, O., Hu, Q., Zhou, X., Zhang, R., Du, Y., Li, M., Ma, L., Xi, S., Fu, W., Xu, Z.-X., et al. (2022). Swinging hydrogen evolution to nitrate reduction activity in molybdenum carbide by ruthenium doping. ACS Catal. *12*, 15045–15055. https://doi.org/10.1021/acscatal.2c04584.

22. Liu, H., Park, J., Chen, Y., Qiu, Y., Cheng, Y., Srivastava, K., Gu, S., Shanks, B.H., Roling, L.T., and Li, W. (2021). Electrocatalytic Nitrate Reduction on Oxide-Derived Silver with Tunable Selectivity to Nitrite and Ammonia. ACS Catal. *11*, 8431–8442. https://doi.org/10.1021/acscatal.1c01525.

23. Cao, L., Li, D., Hu, E., Xu, J., Deng, T., Ma, L., Wang, Y., Yang, X.-Q., and Wang, C. (2020). Solvation structure design for aqueous Zn metal batteries. J. Am. Chem. Soc. *142*, 21404–21409. https://doi.org/10.1021/jacs.0c09794.

24. Guo, Y., Gu, J., Zhang, R., Zhang, S., Li, Z., Zhao, Y., Huang, Z., Fan, J., Chen, Z., and Zhi, C. (2021). Molecular Crowding Effect in Aqueous Electrolytes to Suppress Hydrogen Reduction Reaction and Enhance Electrochemical Nitrogen Reduction. Adv. Energy Mater. *11*, 2101699. https://doi.org/10.1002/aenm.202101699.

25. Sun, P., Ma, L., Zhou, W., Qiu, M., Wang, Z., Chao, D., and Mai, W. (2021). Simultaneous regulation on solvation shell and electrode interface for dendrite-free Zn ion batteries achieved by a low-cost glucose additive. Angew. Chem. *133*, 18395–18403. https://doi.org/10.1002/ange.202105756.

26. Huang, M., Gong, S., Wang, C., Yang, Y., Jiang, P., Wang, P., Hu, L., and Chen, Q. (2021). Lewis-Basic EDTA as a Highly Active Molecular Electrocatalyst for CO_2 Reduction to CH_4. Angew. Chem. Int. Ed. *60*, 23002–23009. https://doi.org/10.1002/anie.202110594.

27. Ramirez, B.L., and Lu, C.C. (2020). Rare-earth supported nickel catalysts for alkyne semihydrogenation: chemo-and regioselectivity impacted by the Lewis acidity and size of the support. J. Am. Chem. Soc. *142*, 5396–5407. https://doi.org/10.1021/jacs.0c00905.

28. Kim, J.-H., Shin, K., Kawashima, K., Youn, D.H., Lin, J., Hong, T.E., Liu, Y., Wygant, B.R., Wang, J., Henkelman, G., and Mullins, C.B. (2018). Enhanced activity promoted by CeO_x on a CoO_x electrocatalyst for the oxygen evolution reaction. ACS Catal. *8*, 4257–4265. https://doi.org/10.1021/acscatal.8b00820.

29. Sun, J., Xue, H., Zhang, Y., Zhang, X.-L., Guo, N., Song, T., Dong, H., Kong, Y., Zhang, J., and Wang, Q. (2022). Unraveling the synergistic effect of heteroatomic substitution and vacancy engineering in $CoFe_2O_4$ for superior electrocatalysis performance. Nano Lett. *22*, 3503–3511. https://doi.org/10.1021/acs.nanolett.1c04425.

30. Theerthagiri, J., Durai, G., Tatarchuk, T., Sumathi, M., Kuppusami, P., Qin, J., and Choi, M.Y. (2020). Synthesis of hierarchical structured rare earth metal-doped Co_3O_4 by polymer combustion method for high performance electrochemical supercapacitor electrode materials. Ionics *26*, 2051–2061. https://doi.org/10.1007/s11581-019-03330-9.

31. Yao, Y., Gao, Z., Lv, Y., Lin, X., Liu, Y., Du, Y., Hu, F., and Zhao, Y.S. (2019). Heteroepitaxial Growth of Multiblock Ln-MOF Microrods for Photonic Barcodes. Angew. Chem. *131*, 13941–13945. https://doi.org/10.1002/ange.201907433.

32. Yao, J., Lu, H., Hou, B., Xiao, Y., Jia, L., Li, D., and Wang, J. (2021). The promotional effect of La dopant on Co_3O_4 catalytic performance towards C_3H_8 combustion. Catal. Lett. *151*, 1745–1754. https://doi.org/10.1007/s10562-020-03429-z.

33. Fan, X., Liu, C., Li, Z., Cai, Z., Ouyang, L., Li, Z., He, X., Luo, Y., Zheng, D., Sun, S., et al. (2023). Pd-doped Co_3O_4 nanoarray for efficient eight-electron nitrate electrocatalytic reduction to ammonia synthesis. Small *19*, 2303424. https://doi.org/10.1002/smll.202303424.

34. Di Valentin, C., Pacchioni, G., Selloni, A., Livraghi, S., and Giamello, E. (2005). Characterization of paramagnetic species in N-doped TiO_2 powders by EPR spectroscopy and DFT calculations. J. Phys. Chem. B *109*, 11414–11419. https://doi.org/10.1021/jp051756t.

35. Chen, D., Zhang, S., Bu, X., Zhang, R., Quan, Q., Lai, Z., Wang, W., Meng, Y., Yin, D., Yip, S., et al. (2022). Synergistic modulation of local environment for electrochemical nitrate reduction via asymmetric vacancies and adjacent ion clusters. Nano Energy *98*, 107338. https://doi.org/10.1016/j.nanoen.2022.107338.

36. Mao, Y., Wang, P., Li, L., Chen, Z., Wang, H., Li, Y., and Zhan, S. (2020). Unravelling the synergy between oxygen vacancies and oxygen substitution in BiO_{2-x} for efficient molecular-oxygen activation. Angew. Chem. Int. Ed. *59*, 3685–3690. https://doi.org/10.1002/anie.201914001.

37. White, B., Banerjee, S., O'Brien, S., Turro, N.J., and Herman, I.P. (2007). Zeta-potential measurements of surfactant-wrapped individual single-walled carbon nanotubes. J. Phys. Chem. C *111*, 13684–13690. https://doi.org/10.1021/jp070853e.

38. Leroy, P., Tournassat, C., and Bizi, M. (2011). Influence of surface conductivity on the apparent zeta potential of TiO_2 nanoparticles. J. Colloid Interface Sci. *356*, 442–453.

39. Weberg, A.B., Murphy, R.P., and Tomson, N.C. (2022). Oriented internal electrostatic fields: an emerging design element in coordination chemistry and catalysis. Chem. Sci. *13*, 5432–5446. https://doi.org/10.1016/j.jcis.2011.01.016.

40. Xu, J., Gao, P., and Zhao, T.S. (2012). Non-precious Co_3O_4 nano-rod electrocatalyst for oxygen reduction reaction in anion-exchange membrane fuel cells. Energy Environ. Sci. *5*,

5333–5339. https://doi.org/10.1039/C1EE01431E.

41. Sun, F., Wang, G., Ding, Y., Wang, C., Yuan, B., and Lin, Y. (2018). NiFe-based metal-organic framework nanosheets directly supported on nickel foam acting as robust electrodes for electrochemical oxygen evolution reaction. Adv. Energy Mater. *8*, 1800584. https://doi.org/10.1002/aenm.201800584.

42. Li, W., Li, F., Yang, H., Wu, X., Zhang, P., Shan, Y., and Sun, L. (2019). A bio-inspired coordination polymer as outstanding water oxidation catalyst via second coordination sphere engineering. Nat. Commun. *10*, 5074. https://doi.org/10.1038/s41467-019-13052-1.

43. Lee, M.W., Kim, M.S., and Kim, K. (1997). Infrared and Raman spectroscopic study of terephthalic acid adsorbed on silver surfaces. J. Mol. Struct. *415*, 93–100. https://doi.org/10.1016/S0022-2860(97)00081-1.

44. Chu, K., Wang, J., Liu, Y.-p., Li, Q.-q., and Guo, Y.-l. (2020). Mo-doped SnS_2 with enriched S-vacancies for highly efficient electrocatalytic N_2 reduction: the critical role of the Mo-Sn-Sn trimer. J. Mater. Chem. *8*, 7117–7124. https://doi.org/10.1039/D0TA01688H.

45. Bae, J., Shin, D., Jeong, H., Kim, B.-S., Han, J.W., and Lee, H. (2019). Highly water-resistant La-doped Co_3O_4 catalyst for CO oxidation. ACS Catal. *9*, 10093–10100. https://doi.org/10.1021/acscatal.9b02920.

46. Li, J.P.H., Zhou, X., Pang, Y., Zhu, L., Vovk, E.I., Cong, L., van Bavel, A.P., Li, S., and Yang, Y. (2019). Understanding of binding energy calibration in XPS of lanthanum oxide by in situ treatment. Phys. Chem. Chem. Phys. *21*, 22351–22358. https://doi.org/10.1039/D0CP90025G.

47. Díez, N., Śliwak, A., Gryglewicz, S., Grzyb, B., and Gryglewicz, G. (2015). Enhanced reduction of graphene oxide by high-pressure hydrothermal treatment. RSC Adv. *5*, 81831–81837. https://doi.org/10.1039/C5RA14461B.

48. Chen, D., Zhang, S., Yin, D., Li, W., Bu, X., Quan, Q., Lai, Z., Wang, W., Meng, Y., Liu, C., et al. (2023). Tailored p-Orbital Delocalization by Diatomic Pt-Ce Induced Interlayer Spacing Engineering for Highly-Efficient Ammonia Electrosynthesis. Adv. Energy Mater. *13*, 2203201. https://doi.org/10.1002/aenm.202203201.

49. Li, R., Rao, D., Hong, X., Zhou, J., Wang, G., Wu, G., Zhu, Z., Han, X., Sun, R., Li, H., et al. (2021). Amorphization-induced surface electronic states modulation of cobaltous oxide nanosheets for lithium-sulfur batteries. Nat. Commun. *12*, 3102. https://doi.org/10.1038/s41467-021-23349-9.

50. Kim, K.-H., Lee, H., Huang, X., Choi, J.H., Chen, C., Kang, J.K., and O'Hare, D. (2023). Energy-efficient electrochemical ammonia production from dilute nitrate solution. Energy Environ. Sci. *16*, 663–672. https://doi.org/10.1039/D2EE03461A.

51. Fang, J.-Y., Zheng, Q.-Z., Lou, Y.-Y., Zhao, K.-M., Hu, S.-N., Li, G., Akdim, O., Huang, X.-Y., and Sun, S.-G. (2022). Ampere-level current density ammonia electrochemical synthesis using CuCo nanosheets simulating nitrite reductase bifunctional nature. Nat. Commun. *13*, 7899. https://doi.org/10.1038/s41467-022-35533-6.

52. Zhang, S., Chen, D., Guo, Y., Zhang, R., Zhao, Y., Huang, Z., Fan, J., Ho, J.C., and Zhi, C. (2023). Piezoelectricity regulated ohmic contact in M/$BaTiO_3$ (M= Ru, Pd, Pt) for charge collision and hydrogen free radical production in ammonia electrosynthesis. Mater. Today *66*, 17–25. https://doi.org/10.1016/j.mattod.2023.03.011.

53. Liu, H., Lang, X., Zhu, C., Timoshenko, J., Rüscher, M., Bai, L., Guijarro, N., Yin, H., Peng, Y., Li, J., et al. (2022). Efficient Electrochemical Nitrate Reduction to Ammonia with Copper Supported Rhodium Cluster and Single-Atom Catalysts. Angew. Chem. *61*, e202202556. https://doi.org/10.1002/anie.202202556.

54. van Langevelde, P.H., Katsounaros, I., and Koper, M.T. (2021). Electrocatalytic nitrate reduction for sustainable ammonia production. Joule *5*, 290–294. https://doi.org/10.1016/j.joule.2020.12.025.

55. Wang, Y., Xu, A., Wang, Z., Huang, L., Li, J., Li, F., Wicks, J., Luo, M., Nam, D.-H., Tan, C.-S., et al. (2020). Enhanced nitrate-to-ammonia activity on copper–nickel alloys via tuning of intermediate adsorption. J. Am. Chem. Soc. *142*, 5702–5708. https://doi.org/10.1021/jacs.9b13347.

56. Svane, K.L., Forse, A.C., Grey, C.P., Kieslich, G., Cheetham, A.K., Walsh, A., and Butler, K.T. (2017). How strong is the hydrogen bond in hybrid perovskites? J. Phys. Chem. Lett. *8*, 6154–6159. https://doi.org/10.1021/acs.jpclett.7b03106.

57. Grinfeld, D., Giannakopulos, A.E., Kopaev, I., Makarov, A., Monastyrskiy, M., and Skoblin, M. (2014). Space-charge effects in an electrostatic multireflection ion trap. Eur. J. Mass Spectrom. *20*, 131–142. https://doi.org/10.1255/ejms.1265.

58. Liu, J.-H., Zhang, Y.-H., Wang, L.-Y., and Wei, Z.-F. (2005). Drawing out the structural information of the first layer of hydrated ions: ATR-FTIR spectroscopic studies on aqueous NH_4NO_3, $NaNO_3$, and $Mg(NO_3)_2$ solutions. Spectrochim. Acta Mol. Biomol. Spectrosc. *61*, 893–899. https://doi.org/10.1016/j.saa.2004.06.030.

59. Pérez-Gallent, E., Figueiredo, M.C., Katsounaros, I., and Koper, M.T. (2017). Electrocatalytic reduction of Nitrate on Copper single crystals in acidic and alkaline solutions. Electrochim. Acta *227*, 77–84. https://doi.org/10.1016/j.electacta.2016.12.147.

60. Rosca, V., Beltramo, G.L., and Koper, M.T. (2004). Hydroxylamine electrochemistry at polycrystalline platinum in acidic media: a voltammetric, DEMS and FTIR study. J. Electroanal. Chem. *566*, 53–62. https://doi.org/10.1016/j.jelechem.2003.11.011.

61. Wang, X., and Andrews, L. (2003). Gold is noble but gold hydride anions are stable. Angew. Chem. *115*, 5359–5364. https://doi.org/10.1002/ange.200351780.

62. Zhu, S., Qin, X., Xiao, F., Yang, S., Xu, Y., Tan, Z., Li, J., Yan, J., Chen, Q., Chen, M., and Shao, M. (2021). The role of ruthenium in improving the kinetics of hydrogen oxidation and evolution reactions of platinum. Nat. Catal. *4*, 711–718. https://doi.org/10.1038/s41929-021-00663-5.

63. Heyes, J., Dunwell, M., and Xu, B. (2016). CO_2 reduction on Cu at low overpotentials with surface-enhanced in situ spectroscopy. J. Phys. Chem. C *120*, 17334–17341. https://doi.org/10.1021/acs.jpcc.6b03065.

64. Iijima, G., Inomata, T., Yamaguchi, H., Ito, M., and Masuda, H. (2019). Role of a hydroxide layer on Cu electrodes in electrochemical CO_2 reduction. ACS Catal. *9*, 6305–6319. https://doi.org/10.1021/acscatal.9b00896.

65. Yao, Y., Zhu, S., Wang, H., Li, H., and Shao, M. (2018). A spectroscopic study on the nitrogen electrochemical reduction reaction on gold and platinum surfaces. J. Am. Chem. Soc. *140*, 1496–1501. https://doi.org/10.1021/jacs.7b12101.

66. Zhang, X., Wang, C., Guo, Y., Zhang, B., Wang, Y., and Yu, Y. (2022). Cu clusters/TiO_{2-x} with abundant oxygen vacancies for enhanced electrocatalytic nitrate reduction to ammonia. J. Mater. Chem. *10*, 6448–6453. https://doi.org/10.1039/D2TA00661H.

67. Gao, W., Xie, K., Xie, J., Wang, X., Zhang, H., Chen, S., Wang, H., Li, Z., and Li, C. (2023). Alloying of Cu with Ru Enabling the Relay Catalysis for Reduction of Nitrate to Ammonia. Adv. Mater. *35*, 2202952. https://doi.org/10.1002/adma.202202952.

68. Ravel, B., and Newville, M. (2005). ATHENA, ARTEMIS, HEPHAESTUS: data analysis for X-ray absorption spectroscopy using IFEFFIT. J. Synchrotron Radiat. *12*, 537–541. https://doi.org/10.1107/S0909049505012719.

69. Zabinsky, S.I., Rehr, J.J., Ankudinov, A., Albers, R.C., and Eller, M.J. (1995). Multiple-scattering calculations of X-ray-absorption spectra. Phys. Rev. B *52*, 2995–3009. https://doi.org/10.1103/PhysRevB.52.2995.

70. Funke, H., Scheinost, A.C., and Chukalina, M. (2005). Wavelet analysis of extended x-ray absorption fine structure data. Phys. Rev. B *71*, 094110. https://doi.org/10.1103/PhysRevB.71.094110.

71. Zhu, D., Zhang, L., Ruther, R.E., and Hamers, R.J. (2013). Photo-illuminated diamond as a solid-state source of solvated electrons in water for nitrogen reduction. Nat. Mater. *12*, 836–841. https://doi.org/10.1038/nmat3696.

72. Green, L.C., Wagner, D.A., Glogowski, J., Skipper, P.L., Wishnok, J.S., and Tannenbaum, S.R. (1982). Analysis of nitrate, nitrite, and [^{15}N] nitrate in biological fluids. Anal. Biochem. *126*, 131–138. https://doi.org/10.1016/0003-2697(82)90118-X.

73. Watt, G.W., and Chrisp, J.D. (1952). Spectrophotometric method for determination of hydrazine. Anal. Chem. *24*, 2006–2008. https://doi.org/10.1016/0003-2697(82)90118-X.

74. Karasawa, N., and Goddard, W.A. (2002). Force fields, structures, and properties of poly (vinylidene fluoride) crystals. Macromolecules *25*, 7268–7281. https://doi.org/10.1021/ma00052a031.

75. Kresse, G., Furthmüller, J., and Hafner, J. (1994). Theory of the crystal structures of

selenium and tellurium: the effect of generalized-gradient corrections to the local-density approximation. Phys. Rev. B *50*, 13181–13185. https://doi.org/10.1103/PhysRevB.54.11169.

76. Kresse, G., and Furthmüller, J. (1996). Efficient iterative schemes for ab initio total-energy calculations using a plane-wave basis set. Phys. Rev. B *54*, 11169–11186. https://doi.org/10.1103/PhysRevB.50.13181.

77. Mortensen, J.J., Hansen, L.B., and Jacobsen, K.W. (2005). Real-space grid implementation of the projector augmented wave method. Phys. Rev. B *71*, 035109. https://doi.org/10.1103/PhysRevB.59.1758.

78. Kresse, G., and Joubert, D. (1999). From ultrasoft pseudopotentials to the projector augmented-wave method. Phys. Rev. B *59*, 1758–1775. https://doi.org/10.1103/PhysRevB.71.035109.

79. Wang, Y., Xu, A., Wang, Z., Huang, L., Li, J., Li, F., Wicks, J., Luo, M., Nam, D.H., Tan, C.S., et al. (2020). Enhanced Nitrate-to-Ammonia Activity on Copper-Nickel Alloys via Tuning of Intermediate Adsorption. J. Am. Chem. Soc. *142*, 5702–5708. https://doi.org/10.1021/acscatal.1c03666.

80. Liu, S., Qian, T., Wang, M., Ji, H., Shen, X., Wang, C., and Yan, C. (2021). Proton-filtering covalent organic frameworks with superior nitrogen penetration flux promote ambient ammonia synthesis. Nat. Catal. *4*, 322–331. https://doi.org/10.1038/s41929-021-00599-w.

81. Haynes, W.M. (2014). CRC Handbook of Chemistry and Physics (CRC press).